Electronic Supplementary Information (ESI) for:

Amorphous Outperforms Crystalline Nanomaterial: Surface Modifications of Molecularly Derived CoP Electro(pre)catalysts for Efficient Water-Splitting

Rodrigo Beltrán-Suito, Prashanth W. Menezes* and Matthias Driess*

Department of Chemistry, Metalorganics and Inorganic Materials, Technische Universität Berlin

*Email: prashanth.menezes@mailbox.tu-berlin.de

*Email: matthias.driess@tu-berlin.de

Table of Contents

Results and Discussion

Materials: The precursor **3** (Fig. S2) was prepared according to literature procedure.[1] The 1,3-diketimine and $CoCl_2.(THF)_{1.5}$ were prepared according to common procedures.[2] Nickel foam (NF) and Fluorine doped tin oxide (FTO, resistivity 8−12 Ωsq^{-1}) were obtained from Racemat BV and Sigma Aldrich respectively.

Synthesis of 2: To a cooled (-30 °C) solution of **1** (4.05 g, 10.35 mmol) in THF (40 ml) was added nBuLi (5.5 mL, 2.5 M in hexane, 13.75 mmol) with stirring. The reaction mixture was allowed to warm to room temperature and stirred further for 3 h. $CoCl_2.(THF)_{1.5}$ (2.44 g, 10.25 mmol) was added and the mixture was refluxed overnight. After cooled to room temperature, 10 mL toluene and 1.92 g KC_8 (14.20 mmol) were added. The reaction mixture was further stirred for 17 h and the colour of the resulted mixture turned to dark red. Volatiles were removed *in vacuo*, and the residue was extracted with diethyl ether (3x25 mL). After filtration and concentration, the saturated solution was cooled to -20 °C for 24 h, **2** crystallized from the solution as dark red crystals (3.66 g, 6.77 mmol, 66 %).

Synthesis of 3: To a solution of **2** (1.10 g, 2.04 mmol) in toluene (20 mL), white phosphorus (P_4) (0.126 g, 1.01 mmol) was added at room temperature. After stirring for 3 h, the colour of the solution changed from dark red to dark pink and a dark brown red precipitate of **3** formed. After filtration, the precipitate was collected and dried under reduced pressure to give the first crop of the title complex as a dark brown solid. Concentration of the filtrate and cooled to -20 °C for 2 days afforded the second crop as dark brown crystals. The combined isolated yield amounted 0.74 g (0.74 mmol, 72 %). Elemental analysis (%): calculated for $C_{54}H_{74}N_4Co_2P_4$: C, 63.53; H, 7.31; N, 5.49. Found: C, 62.77; H, 8.73; N, 7.52. IR (cm^{-1}): v = 556 (w), 606 (w), 668 (w), 738 (m), 755(m), 774 (w), 798 (w), 1058 (w), 1091 (w), 1106 (w), 1197 (w), 1242 (w), 1255 (w), 1290 (s), 1319 (w), 1360 (w), 1380 (w), 1433 (s), 1461 (m), 1502 (m), 1565 (m), 2862 (w), 2923 (w), 2956 (s), 3067 (w). ^{1}H NMR (C_6D_6, 300K) δ (ppm): s 16.42 (3.68, 4H), d 9.72 (8.00, 8 H, $^1J_{H-H}$ = 7.52 Hz), t 5.43 (4.34, 4 H, $^1J_{H-H}$ = 7.38 Hz), s 3.98 ppm (7.58, 8 H) s 1.34 ppm (25.97, 24 H), s 1.06 ppm (25.72, 24 H), s -24.14 ppm (1.51, 1 H).

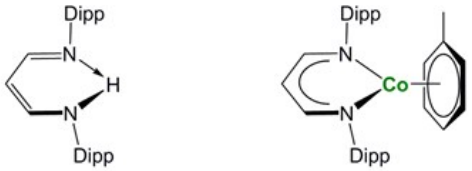

1 **2**

Fig. S1 Molecular structures of 1,3-diketimine ligand (L^{Dipp}, Dipp = 2,6-$^{i}Pr_2C_6H_3$) and 1,3-diketiminato cobalt (I) toluene complex ($L^{Dipp}Co^{I}$(tol)).

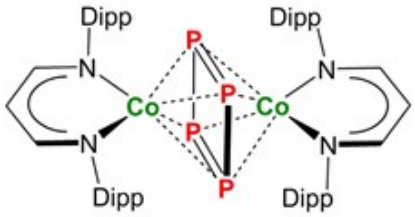

3

Fig. S2 Molecular precursor $L^{Dipp}CoP_4CoL^{Dipp}$. The complex bears a cyclo P_4 structure.

Cyclic Voltammetry Measurement (for molecular precursor): Cyclic voltammetry (CV) measurements of the molecular precursor were performed in a standard three-electrode electrochemical cell having Pt-wire used as an auxiliary electrode, glassy carbon (3 mm diameter) as working electrode and Ag/Ag^{+} as a pseudo reference electrode at 295 K using a Biologic SP-150 potentiostat. All cyclic voltammograms were referenced against the Cp_2Fe/Cp_2Fe^{+} redox couple (Fc/Fc^{+}), which was used as an internal standard. 0.3 M tetrabutyl ammonium hexaflurophosphate ($TBAPF_6$) in THF was used as an electrolyte. The iR-drop was determined and compensated by using the impedance measurement technique implemented in the EC-Lab Software V10.37.

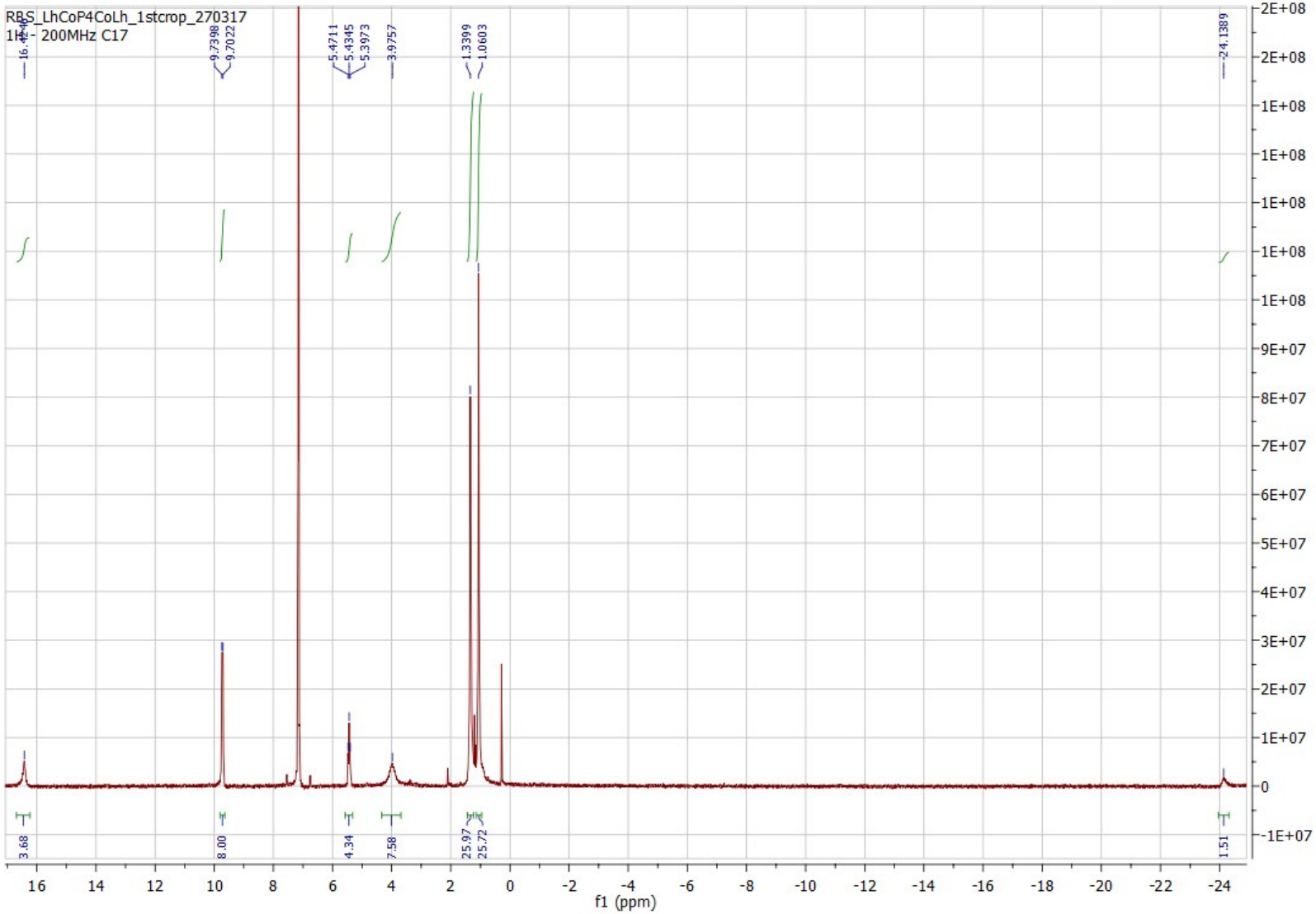

Fig. S3 ^{1}H-NMR of the molecular precursor in THF-d_8. Signal assignments and integrations are shown on **Synthesis of 3** (Page S2).

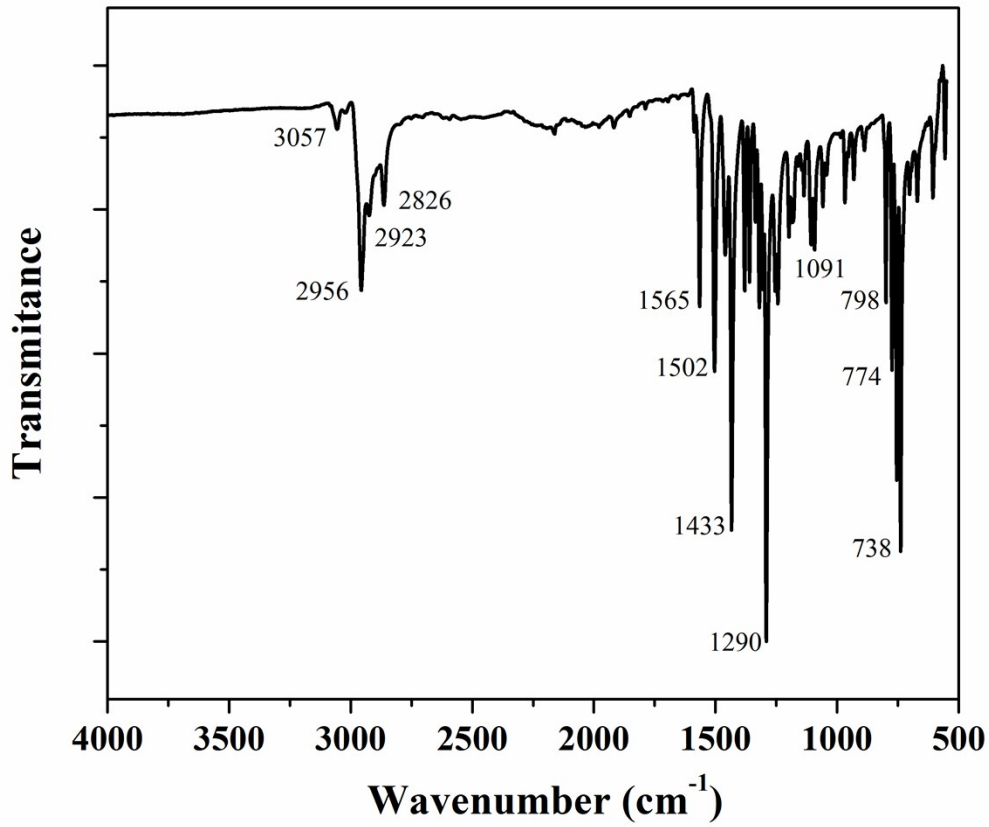

Fig. S4 FTIR of **3** under N_2. All observed bands are consistent with the reported complex.[1]

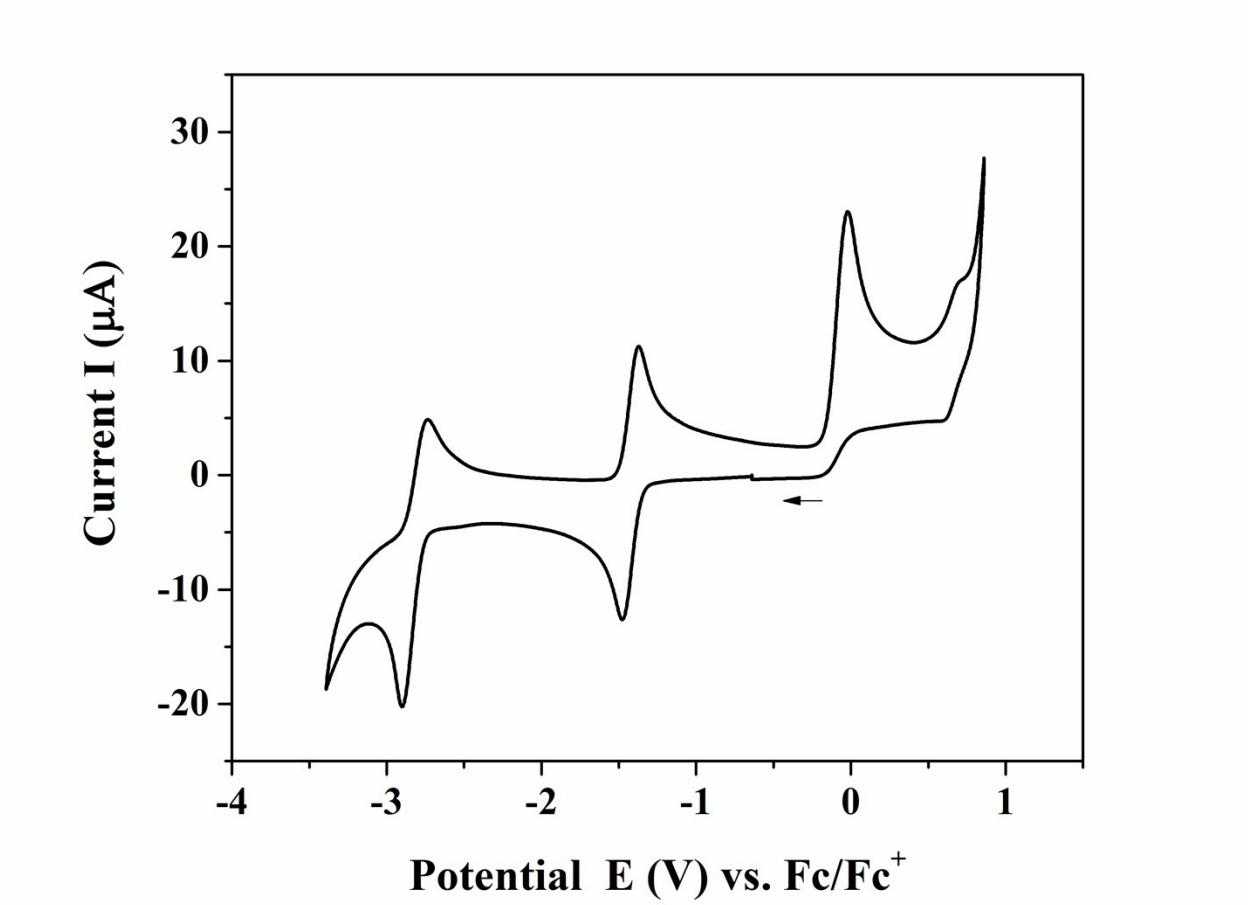

Fig. S5 CV of molecular precursor **3** (1 mM in THF/ 0.3 M $TBAPF_6$). It shows two reversible redox events at $E_{1/2}$ = -1.42 V (vs. Fc/Fc^+) and $E_{1/2}$ = -2.81 V (vs. Fc/Fc^+) and one irreversible event at E_{pa} = -0.03 V (vs Fc/Fc^+) at a scan rate of v = 100 mVs^{-1}.

The reversibility of the redox events was confirmed by recording the CV at different scan rates from 50 to 800 mVs^{-1} (see Fig. S6 and Fig. S7).

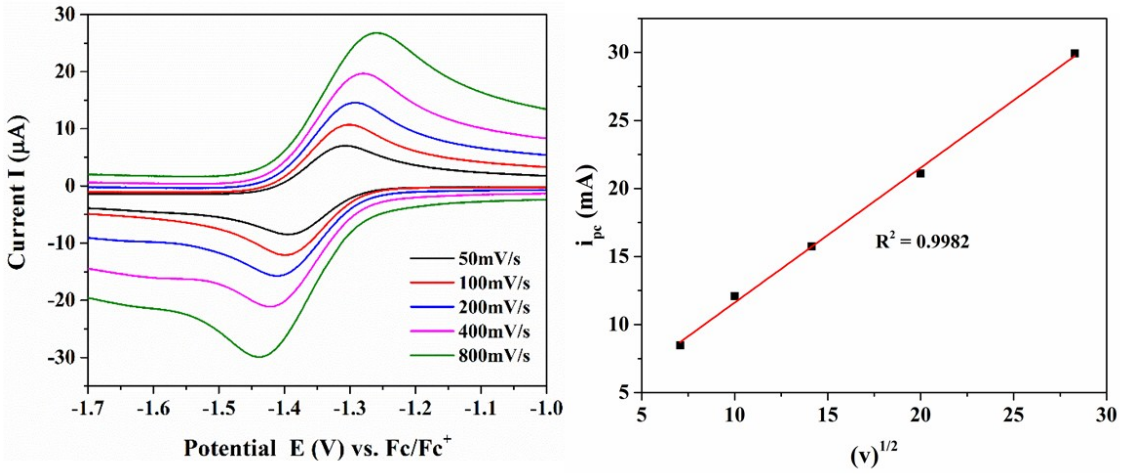

Fig. S6 CV of precursor **3** (1 mM in THF/ 0.3 M $TBAPF_6$) centered at -1.42 V and recorded at different scan rates (50-800 mVs^{-1}) (left). The plot of forward peak current vs. square root of scan rates (right).

Table S1 Electrochemical data for the reversibility of the redox couple at $E_{1/2}$ = -1.42 V (vs. Fc/Fc^+) for **1**.

v (mVs^{-1})	E_{pc} (V)	E_{pa} (V)	ΔE_p (V)	i_{pc} (μA)	i_{pa} (μA)	i_{pa}/i_{pc}	$i_{pc}/(v^{1/2})$
50	-1.393	-1.307	86	8	7	0.83	1.20
100	-1.399	-1.301	98	12	11	0.89	1.21
200	-1.411	-1.292	119	16	15	0.93	1.11
400	-1.423	-1.280	143	21	20	0.93	1.06
800	-1.439	-1.258	181	30	27	0.90	1.06

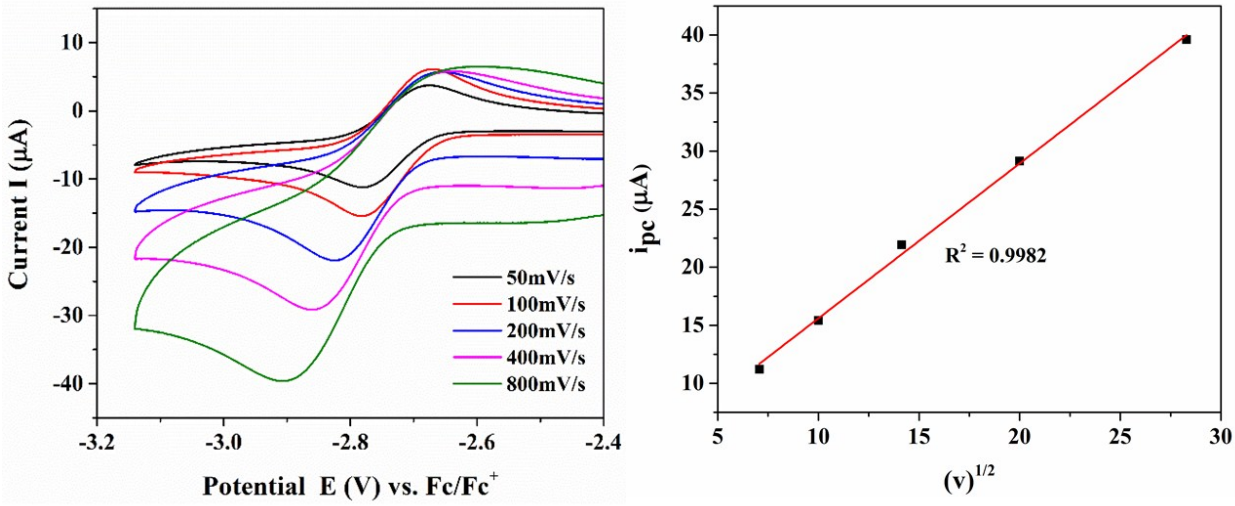

Fig. S7 CV of precursor **3** (1 mM in THF/ 0.3 M $TBAPF_6$) centered at -2.81 V and recorded at different scan rates (50-800 mVs^{-1}) (left). The plot of forward peak current vs. square root of scan rates (right).

Table S2 Electrochemical data for the reversibility of the redox couple at $E_{1/2}$ = -2.81 V (vs. Fc/Fc^+) for **3**.

v (mVs^{-1})	E_{pc} (V)	E_{pa} (V)	ΔE_p (V)	i_{pc} (μA)	i_{pa} (μA)	i_{pa}/i_{pc}	$i_{pc}/(v^{1/2})$
50	-2.781	-2.675	106	11	4	0.33	1.59
100	-2.781	-2.672	110	15	6	0.40	1.54
200	-2.824	-2.655	169	22	6	0.26	1.55
400	-2.860	-2.637	223	29	6	0.20	1.46
800	-2.908	-2.597	311	40	6	0.16	1.40

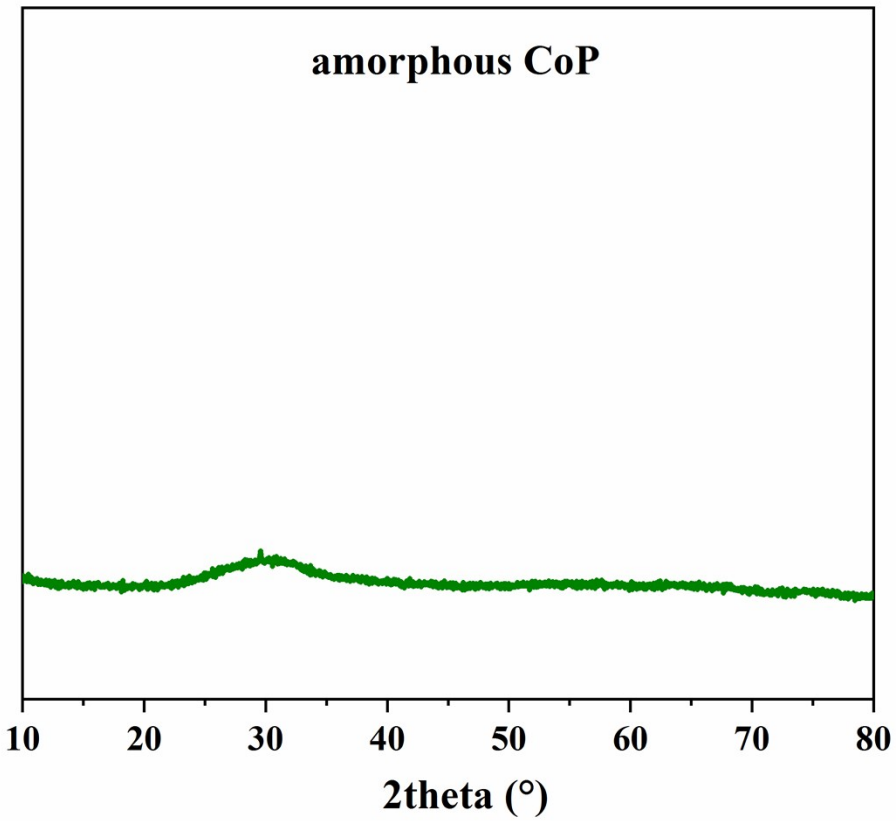

Fig. S8 Powder X-ray diffraction pattern of amorphous CoP. The obtained spectra did not reveal any sharp reflection, displaying the amorphous nature of the produced material. The amorphousness of the phase was additionally confirmed by the selected area diffraction pattern (SAED) (see Fig. 1, main text). Moreover, the composition of the material was also confirmed by EDX, XPS and ICP-AES analysis.

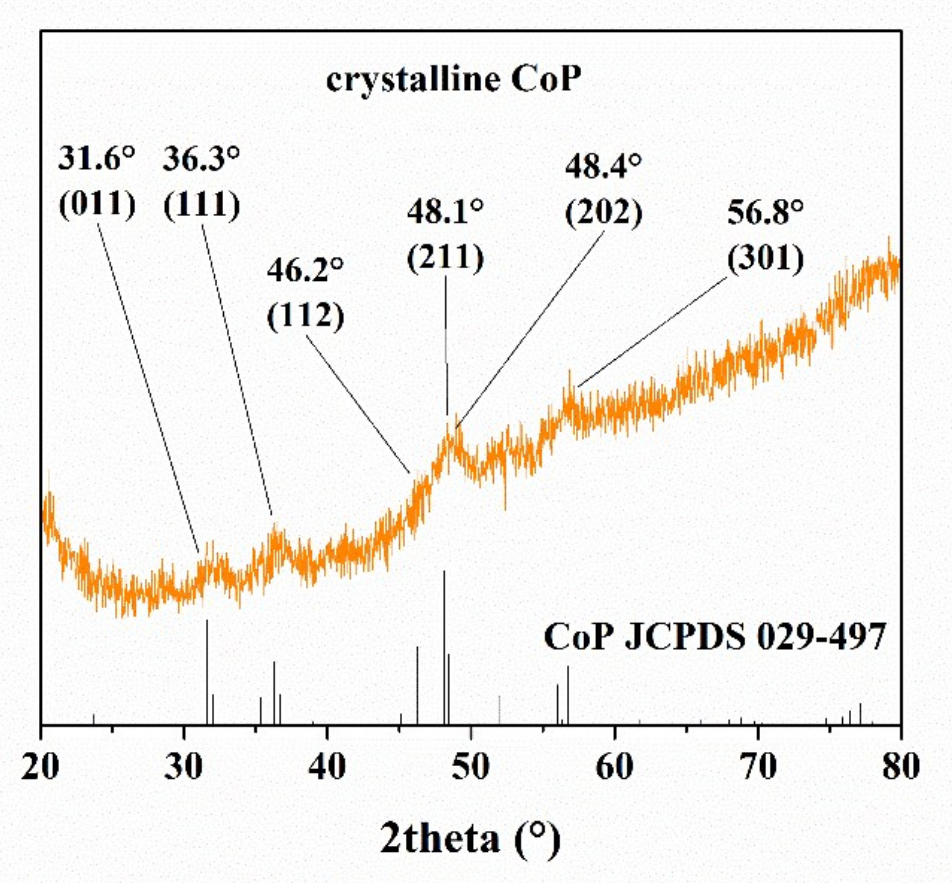

Fig. S9 PXRD pattern of crystalline CoP. The observed main diffraction peaks and their corresponding Miller indices are in accordance with the literature reported CoP (JCPDS 29-0497). The broad reflections can be attributed to the small particle size of CoP nanostructures. The crystallinity of the material and the phase confirmation was further studied by SAED (see Fig. 1 on main text). Moreover, the composition of the CoP material was also confirmed by EDX, XPS and ICP-AES analysis.

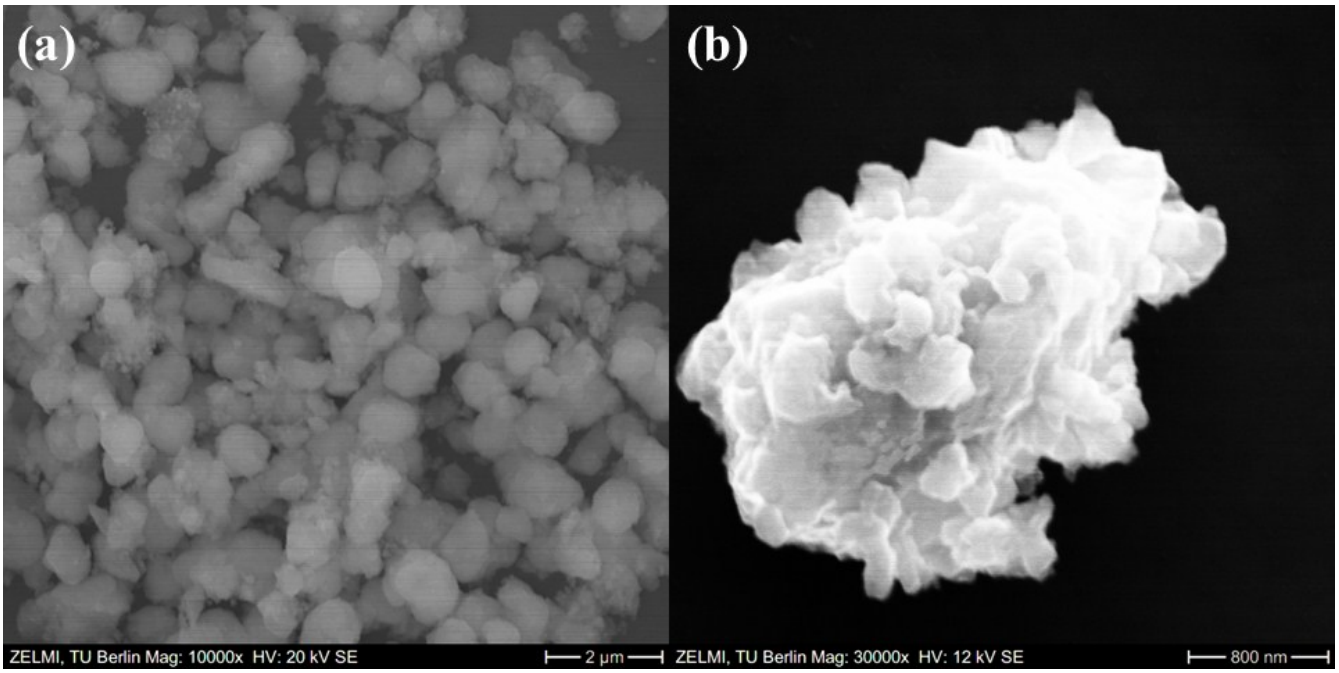

Fig. S10 SEM images showing agglomerations of particles of (a) amorphous CoP (scale bar 2µm) and (b) crystalline CoP (scale bar 800 nm).

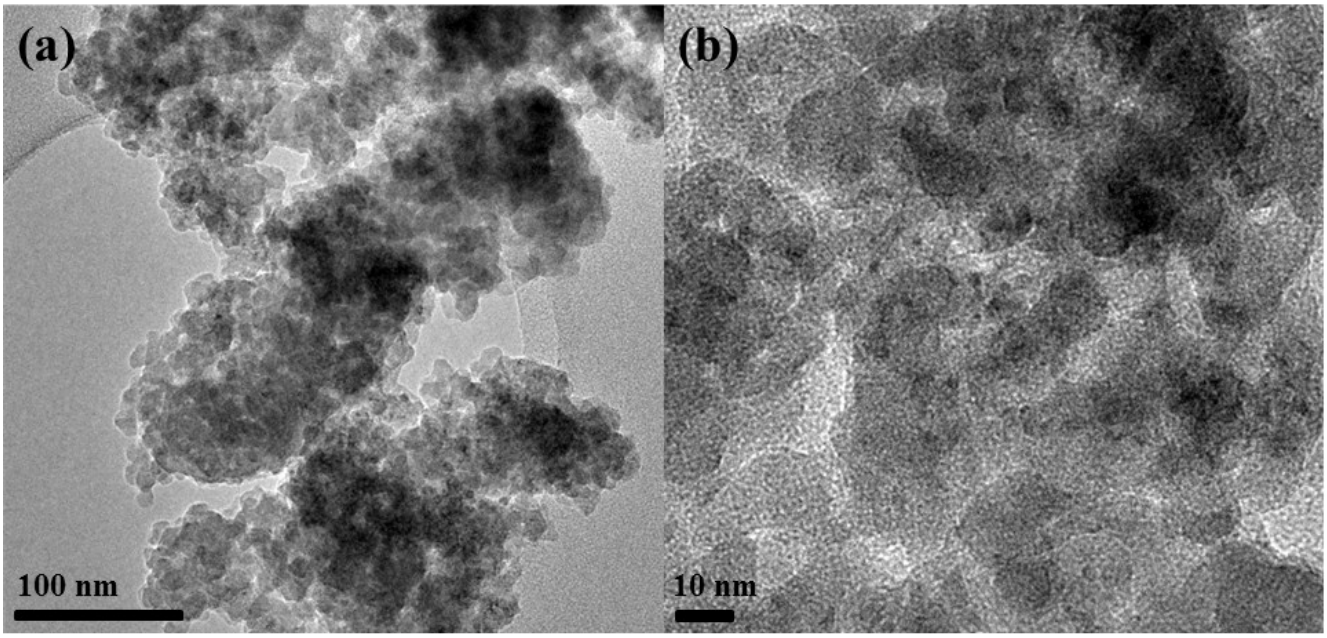

Fig. S11 TEM image of (a) amorphous CoP and (b) high-resolution HR-TEM image. The HR-TEM shows the presence of nanoparticles of ~10nm size that forming larger aggregates.

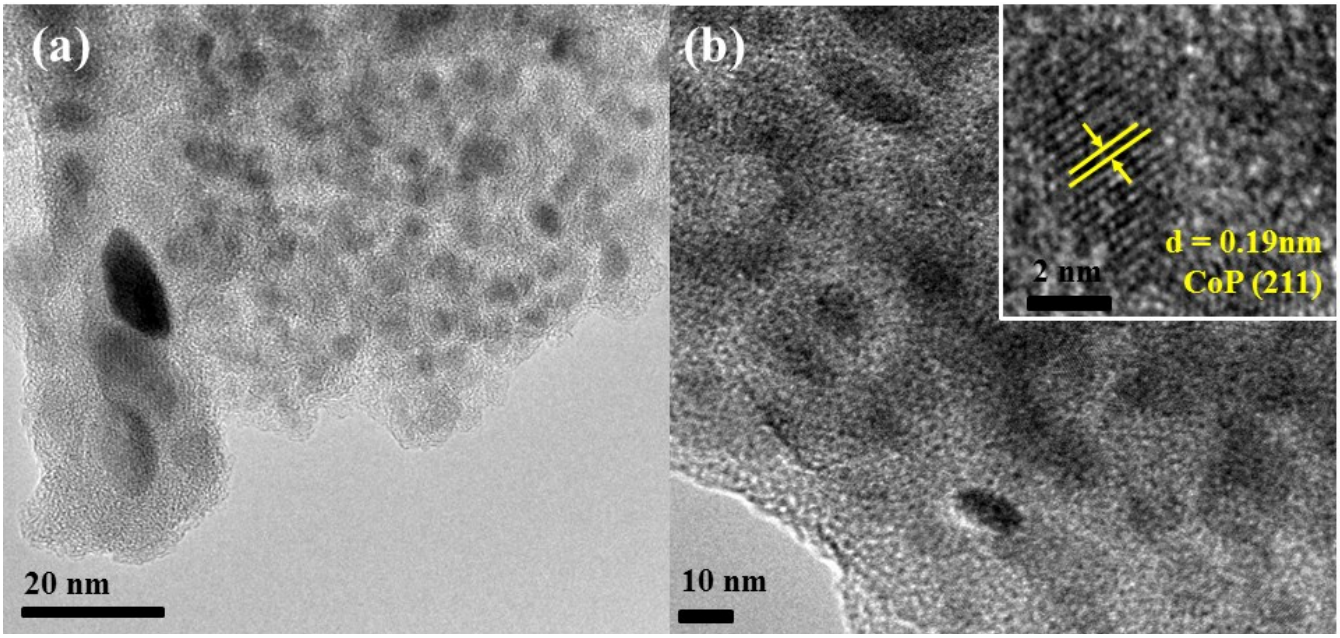

Fig. S12 (a) The TEM image and (b) HR-TEM image of crystalline CoP. The TEM image shows agglomeration of small crystalline particles (> 4 nm). The inset on (b) shows clear crystalline fringes associated with the lattice spacing of 0.19 nm corresponding to the (211) plane of the CoP phase.

Table S3 Determination of the Co and P content in the prepared materials by ICP-AES. Three independent measurements were performed, and the average data is shown.

Material	Co:P (ICP-AES)
Crystalline CoP	1:1.14
Amorphous CoP	1:1.05

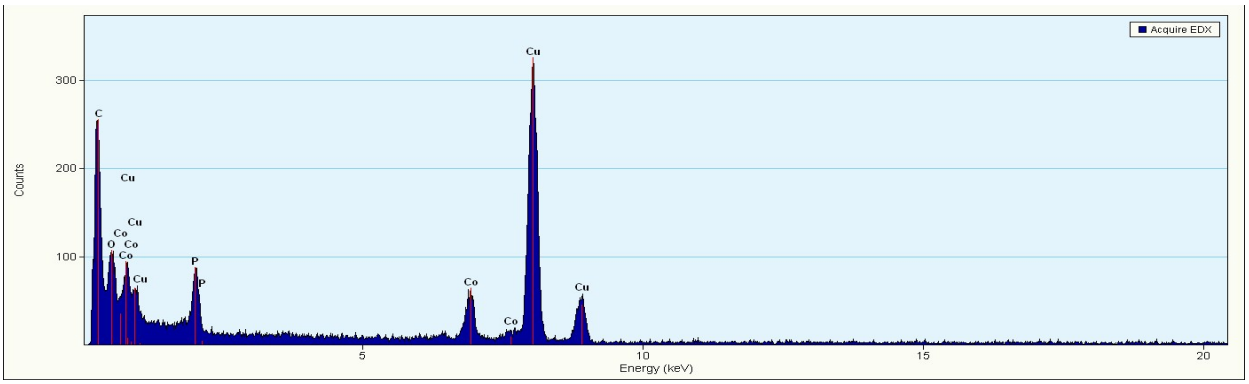

Fig. S13 EDX of amorphous CoP, which confirms the presence of Co and P. The presence of Cu peaks is due to the TEM grid (carbon film on 300 mesh Cu-grid). The EDX values of Co:P were ~1:1.

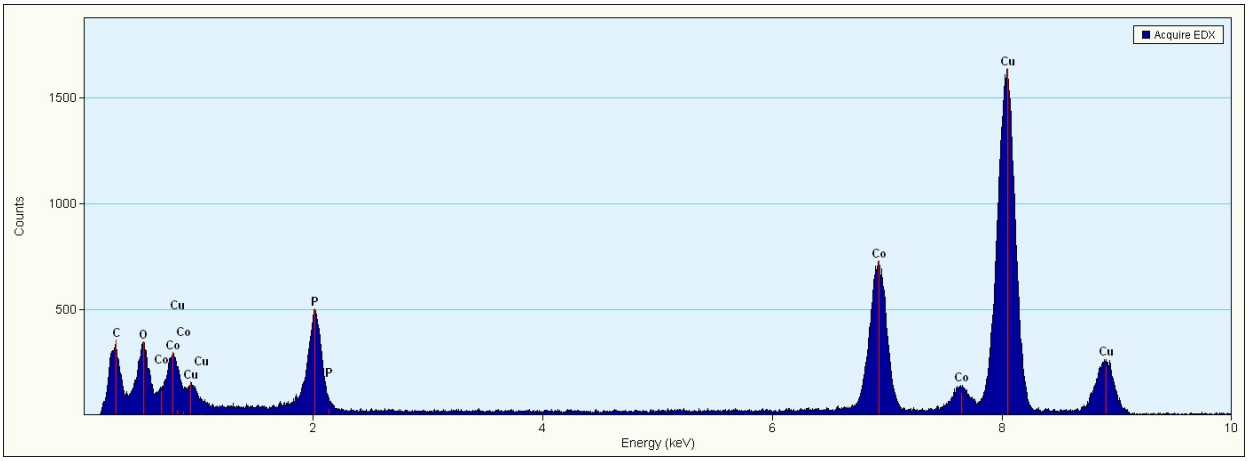

Fig. S14 EDX of crystalline CoP, which confirms the presence of Co and P. The presence of Cu peaks is due to the TEM grid (carbon film on 300 mesh Cu-grid). The EDX values of Co:P were ~1:1.

Table S4 Determination of C, H and O content by elemental analysis. The presence of C, H and N arise from the β-diketiminato ligand of the precursor.

Material	%C	%H	%N
Amorphous CoP	6.49	0.61	0.98
Crystalline CoP	7.23	0.29	0.27

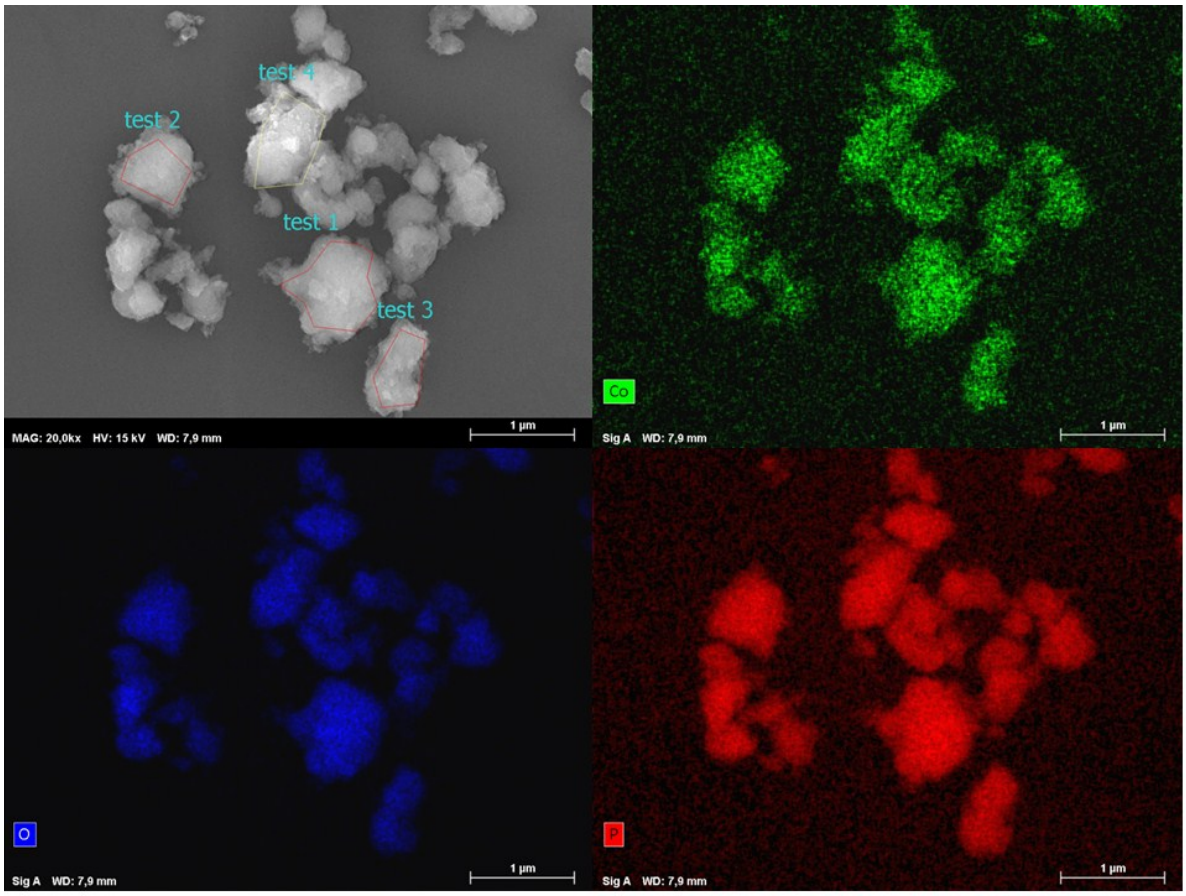

Fig. S15 Elemental mapping of Co (green, top right), P (red, bottom right) and O (blue, bottom left) on amorphous CoP prepared by hot injection. The used substrate was silicon wafer. Homogenous distribution of Co and P was observed in the material particles and the presence of O is due to the surface passivation (scale bar 1 µm).

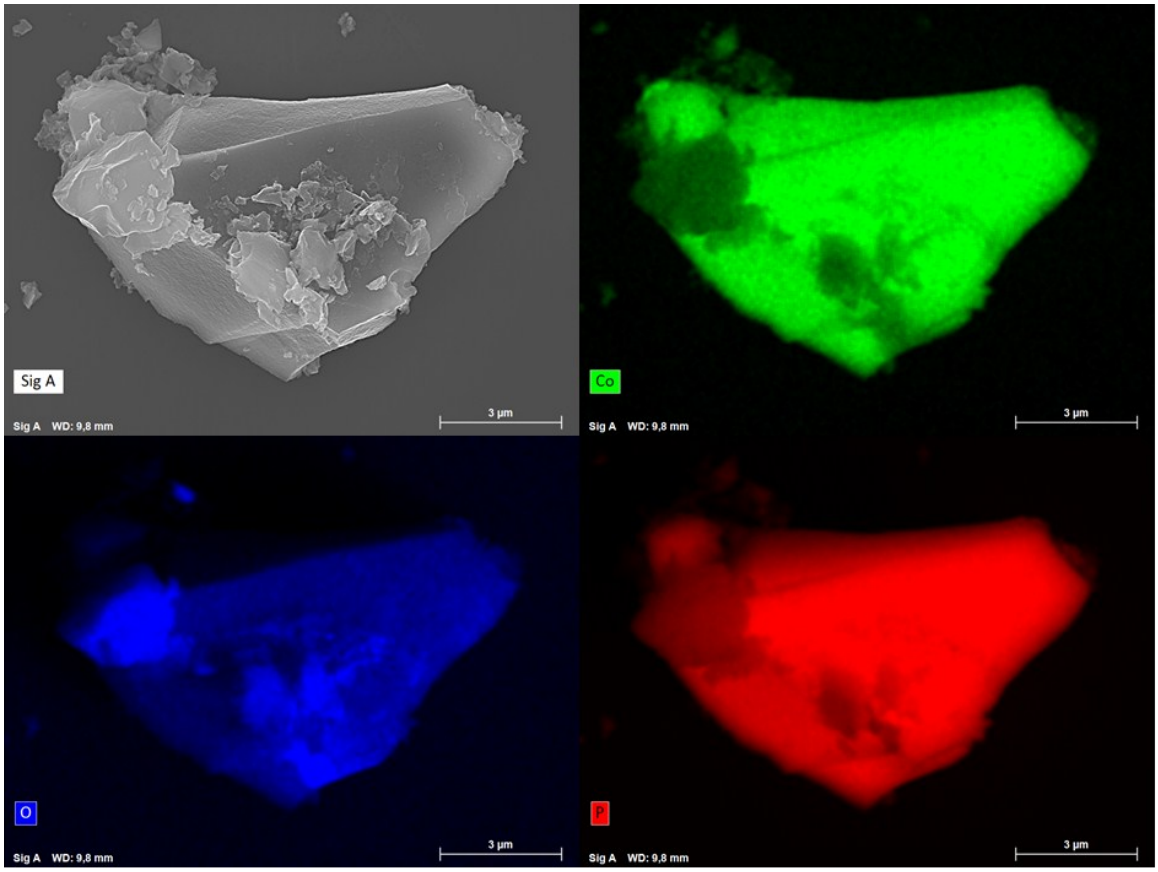

Fig. S16 Elemental mapping of Co (green, top right), P (red, bottom right), O (blue, bottom left) and on crystalline CoP prepared by pyrolysis. Homogenous distribution of Co and P was observed in the material particles and the presence of O is due to the surface passivation (scale bar 3 µm).

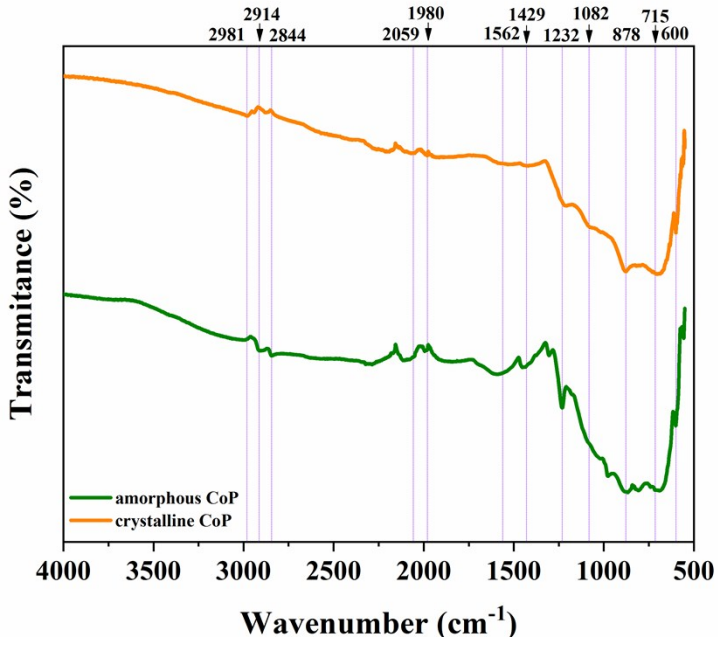

Fig. S17 FTIR of amorphous and crystalline CoP. Both materials showed small bands between 1250 and 500 cm^{-1} which could correspond to the stretching and bending vibrations of the phosphate group, originated from surface oxidation.[3,4] The small peak around 600 cm^{-1} which appears on both materials is characteristic of the Co-O bond, which may be present as the samples contain oxygen.[4] The attained FTIR spectra is in accordance with the other CoP based materials.

Table S5 Surface area values obtained from BET experiment.

Material	Surface area (m^2g^{-1})
Crystalline CoP	27.50
Amorphous CoP	28.41

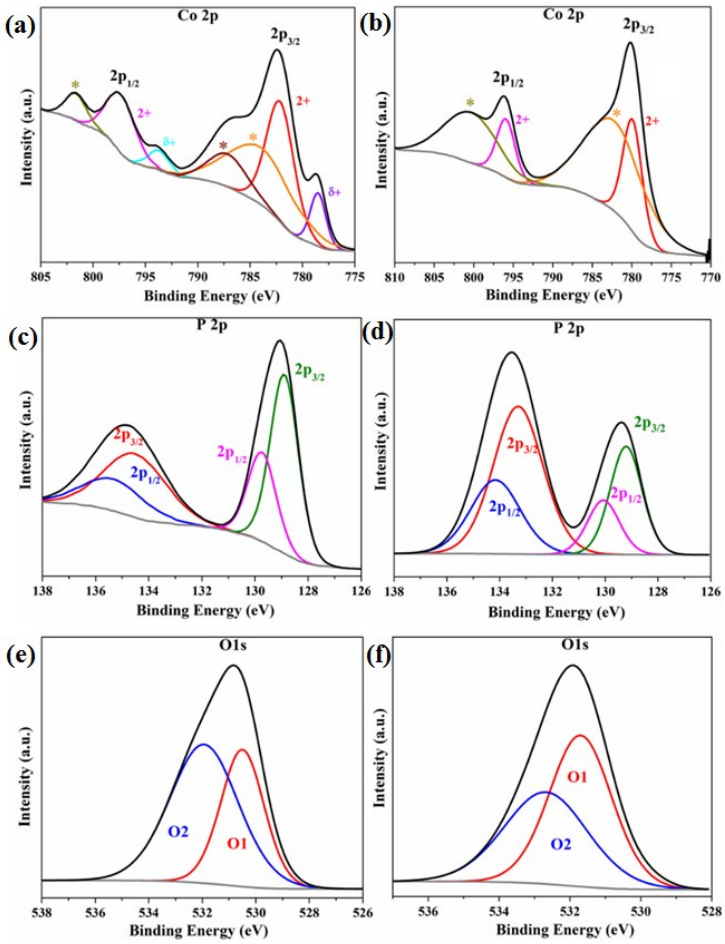

Fig. S18 High-resolution XPS spectra for Co 2p (top), P 2p (centre) and O 1s (bottom) for the as-prepared amorphous (left) and crystalline (right) CoP. The high-resolution Co 2p spectrum (Fig. S18a) of amorphous CoP depicts peaks at 778.7 eV ($2p_{3/2}$) and 793.9 eV ($2p_{1/2}$) which are assigned to the positively charged $Co^{\delta+}$ in CoP.[5] The peaks at 782.2 eV and 797.8 eV, as well as their two satellites (at 787.5 eV and 801.8 eV), correspond to the presence of Co^{2+}.[6] The P 2p spectrum of the amorphous CoP (Fig. S18c) shows a peak at 129.0 eV which is related to the negatively charged $P^{\delta-}$ in phosphide.[3] The less intense peak at 134.9 eV is attributed to phosphate (PO_4^{3-}) species. The oxidation of Co or P was originated from surface oxidation which is very hard to avoid in phosphide-based materials as reported in the literature.[3,7] The high-resolution O 1s spectrum (Fig. S18e) was also deconvoluted into two peaks: 530.5 eV and 531.9 eV. The former peak can be assigned to the O species in Co-O-P and the latter to P=O.[3,8] In the case of the crystalline material, the Co 2p spectrum (b) shows that the majority of cobalt is present as Co^{2+} (780.0 eV and 796.0 eV) indicating the surface of the particle is strongly oxidized under aerial conditions.[6] The P 2p spectrum (d) shows two peaks: 129.4 eV, related to $P^{\delta-}$ and a slightly higher intense peak at 133.6 eV is attributed to phosphate.[3,7] Finally, the high-resolution O 1s (f) show a major peak (531.9 eV) which was deconvoluted into two peaks at 531.7 eV (O in Co-O-P) and 532.7 eV (P=O).[3,8]

Table S6 Activity comparison of as-prepared CoP materials with other highly efficient non-noble transition metal-based catalysts at 1 M KOH for OER.

Catalyst	Current density ($mAcm^{-2}$)	Overpotential η (mV)	Reference
Amorphous CoP/NF	**10**	**284**	**This work**
	100	**341**	**This work**
Crystalline CoP/NF	**10**	**305**	**This work**
	100	**392**	**This work**
Amorphous CoP/FTO	**10**	**360**	**This work**
	100	**414**	**This work**
Crystalline CoP/FTO	**10**	**414**	**This work**
	100	**592**	**This work**
IrO_2/NF	**10**	**287**	**This work**
	100	**413**	**This work**
IrO_2/FTO	**10**	**409**	**This work**
	100	**-**	**This work**
Pt	**10**	**654**	**This work**
	100	**-**	**This work**
Co_3O_4/ $NiCo_2O_4$ DSNCs	10	340	[9]
CoCo LDH	10	393	[10]
NiFe-LDH	10	300	[10]
NiCo-LDH	10	335	[10]
$Ni_{11}(HPO_3)_8(OH)_6$/NF	10	232	[11]
NiFe oxides	10	300	[12]
FeCoW oxy-hydroxides	10	191	[13]
Co_3O_4/Au	10	400	[14]
$CoCr_2O_4$	10	422	[15]
$CoCr_2O_4$/CNT	10	326	[15]
FeNi-rGO LDH	10	195	[16]
FeNi-GO LDH	10	210	[16]
CoS	10	361	[17]
$(Ni,Co)Se_{0.85}$-NiCo LDH	10	216	[18]

Table S7 Activity comparison of as-prepared CoP materials with other highly active non-noble transition metal phosphide-based catalysts at 1 M KOH for OER.

Catalyst	Current density ($mAcm^{-2}$)	Overpotential η (mV)	Reference
Amorphous CoP/NF	**10**	**284**	**This work**
	100	**341**	**This work**
Crystalline CoP/NF	**10**	**305**	**This work**
	100	**392**	**This work**
FeCoNiP	10	200	[19]
Ni_2P	10	290	[20]
Ni-P	10	300	[21]
Ni_2P/FTO	10	400	[20]
Ni_2P/Ni/NF	10	200	[22]
Ni_xP_y-325	10	320	[23]
Ni-P film	10	344	[24]
FeP/Au	10	290	[25]

Table S8 Activity comparison of as-prepared CoP materials with reported cobalt phosphide-based catalysts at 1 M KOH for OER.

Catalyst	Current density ($mAcm^{-2}$)	Overpotential η (mV)	Reference
Amorphous CoP/NF	**10**	**284**	**This work**
	100	**341**	**This work**
Crystalline CoP/NF	**10**	**305**	**This work**
	100	**392**	**This work**
Surface phosphate modified cobalt phosphide nanorod bundles	10	310	[3]
Cobalt-Phosphide Nanorods	10	320	[7]
Fe-Ni-P hybrid catalyst	10	154	[26]
Co_2P/GCE	10	370	[27]
CoMnP	10	330	[27]
Cobalt phosphide/carbon dots composite	10	400	[28]
cobalt-rich cobalt phosphide catalysts	10	319	[29]
Nanostructured cobalt phosphide-based films	10	340	[30]
Porous Cobalt Phosphide Polyhedrons	10	289	[31]
Core-Oxidized Amorphous Cobalt Phosphide Nanostructures	10	287	[32]
CoP nanowie on Ti mesh	10	310	[33]
CoP hollow polyhedron	10	400	[34]
Co/Co_2P nanoparticles/NF	50	190	[35]
Co-P/NC nano-Polyhedrons	10	319	[36]
Cobalt-phosphorus derived films/Cu	10	345	[37]

CoP mesoporous rods	10	290	[38]
Porous Co-based phosphide/phosphate thin film	30	330	[39]

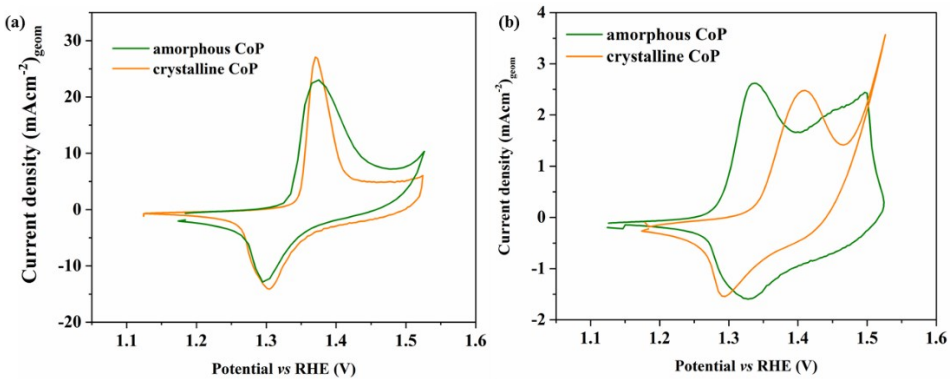

Fig. S19 CV (scan rate 10 mVs^{-1}, iR compensation at 85 %) of amorphous and crystalline CoP and on (a) NF and on (b) FTO measured between 1.12 V and 1.52 V (vs RHE) in 1 M KOH. The materials on both substrates featured a pair of anodic and cathodic peaks corresponding to the reaction of oxidation of the cobalt hydroxide in alkaline media: $Co(OH)_2 + OH^- \rightarrow CoOOH + H_2O + e^-$. Eventually, the produced CoOOH could be furtherly oxidized to the CoO_2 during anodic polarization: $CoOOH + OH^- \rightarrow CoO_2 + H_2O + e^-$.[40] These peaks have been also often observed for most of the first-row transition-metal-based materials, which exhibit $M(OH)_2$/MOOH phase formation at potentials between ca. 1.1 V and 1.4 V (vs NHE).[40]

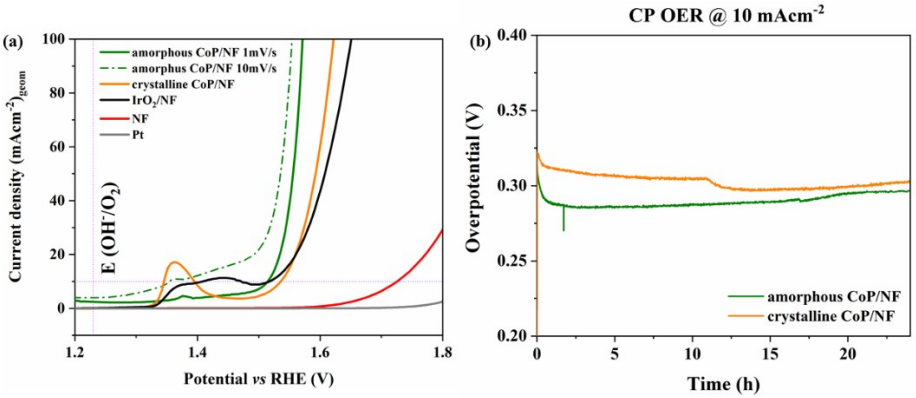

Fig. S20 (a) Polarization curves of OER of different CoP materials and commercial noble metal-based catalysts deposited on NF with a scan rate of 10 mVs^{-1} in 1 M KOH (iR compensation at 85 %). The overpotential at 10 $mAcm^{-2}$ of amorphous CoP could not be determined with the curve at scan rate of 10 mVs^{-1}. A new polarization curve with a scan rate of 1 mVs^{-1} was finally done to determine it. (b) Chronopotentiometry (CP) experiment of amorphous and crystalline CoP on NF measured in OER conditions at a constant current of 10 $mAcm^{-2}$ in 1 M KOH for 24 h.

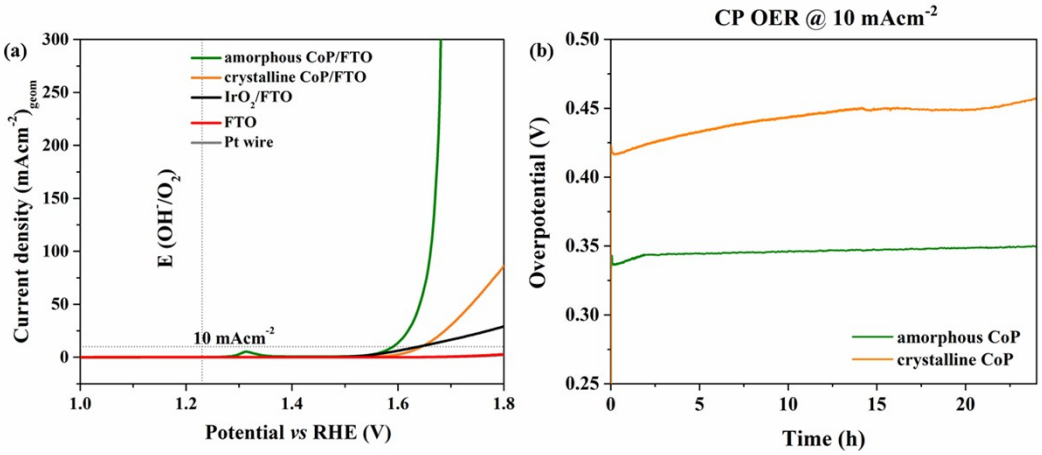

Fig. S21 (a) The CoP catalysts were also deposited on FTO and polarization experiments for OER were conducted in 1 M KOH solution that was then compared to IrO_2/FTO, bare FTO and Pt. The activity of the materials follows the same trend found in NF. Scan rate: 10 mVs^{-1}, iR compensation: 85 %. The stability was also investigated through chronopotentiometry (b) by applying a current of 10 $mAcm^{-2}$ for 24 h. The amorphous CoP remained very stable whereas a decrease in overpotential resulted for crystalline CoP.

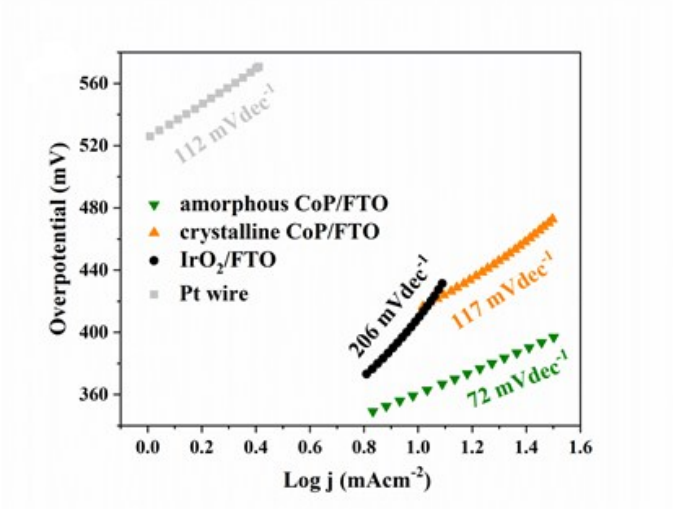

Fig. S22 Tafel plot for OER for the as-prepared CoP materials deposited on FTO, IrO_2/FTO and Pt in aqueous 1 M KOH solution in OER. Scan rate: 1 mVs^{-1}. The amorphous CoP shows the lowest Tafel slope (72 $mVdec^{-1}$), which surpasses the crystalline CoP (117 $mVdec^{-1}$) and the state-of-the-art IrO_2/FTO (206 $mVdec^{-1}$) and the Pt wire (112 $mVdec^{-1}$).

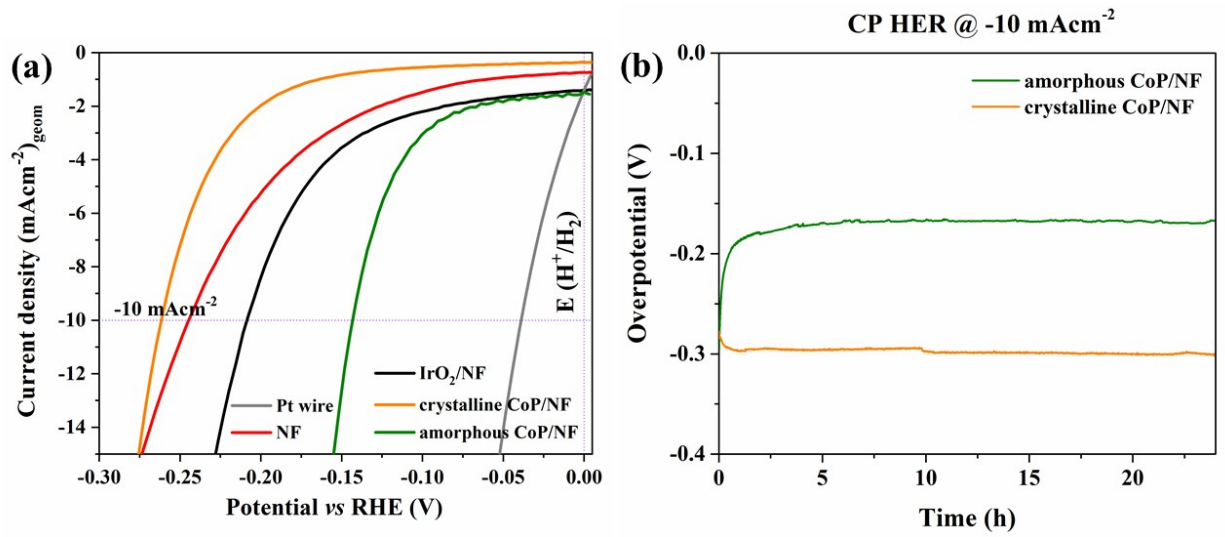

Fig. S23 (a) Polarization curves of HER of different CoP materials and commercial noble metal-based catalysts deposited on NF with a scan rate of 10 mVs^{-1} in 1 M KOH (iR compensation at 85 %). (b) Chronopotentiometric experiments for HER (1 M KOH on NF) for amorphous and crystalline CoP on NF were investigated by applying a current of 10 $mAcm^{-2}$ for 24 h. Both samples exhibited stable activities over 24 h.

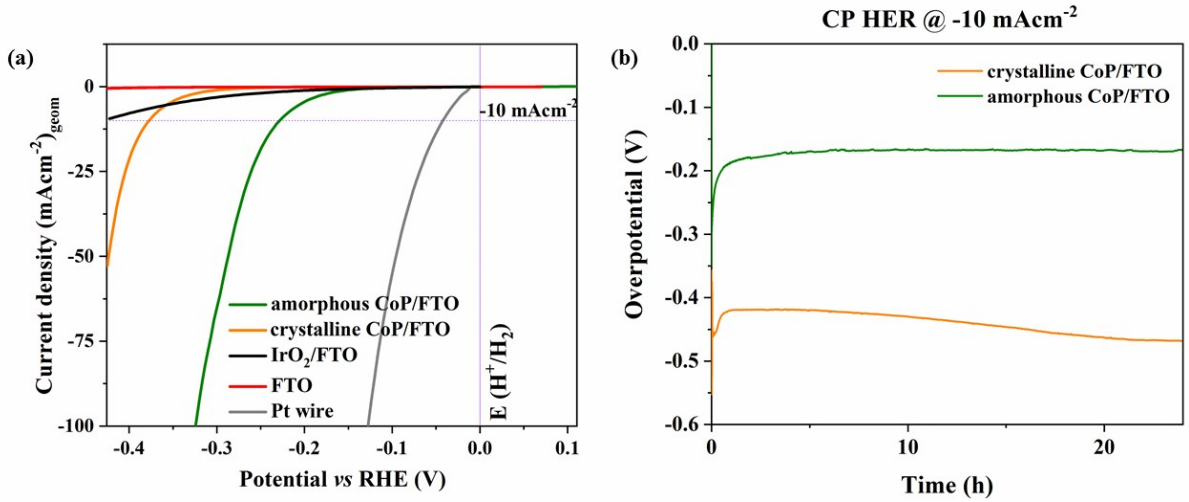

Fig. S24 (a) HER polarization curves on 1 M KOH (left) of amorphous and crystalline CoP, IrO_2 deposited on FTO along with, Pt wire and bare FTO. Both materials show similar activity, with lower overpotentials than IrO_2 and the bare substrate, but higher than Pt. Scan rate: 10 mVs^{-1} (iR compensation at 85 %). (b) Chronopotentiometric experiments for HER (1 M KOH on FTO) of amorphous and crystalline CoP were carried out by applying a constant current of 10 $mAcm^{-2}$ for 24 h. The crystalline CoP showed a continuous decrease in overpotential during the 24 h experiment in comparison to the amorphous CoP, which was stable throughout the experiment.

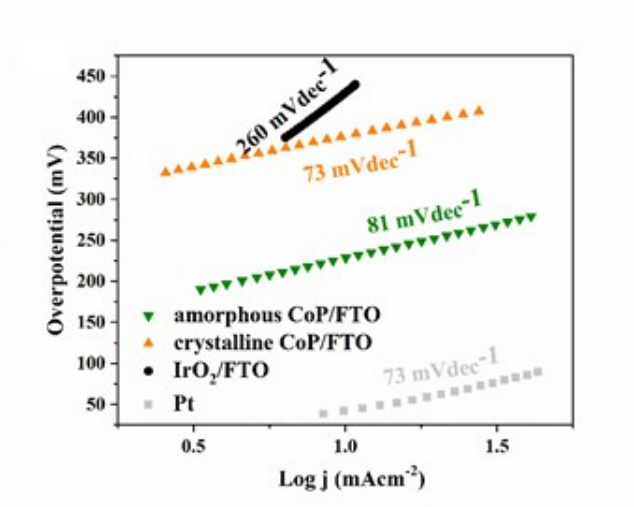

Fig. S25 Tafel plot for HER for the as-prepared CoP materials deposited on FTO, IrO_2/FTO and Pt in aqueous 1 M KOH solution in HER. Scan rate: 1 mVs^{-1}. The crystalline CoP shows a Tafel slope that is comparable to the state-of-the-art Pt catalyst (73 $mVdec^{-1}$). The amorphous CoP showed a slightly lower Tafel slope (81 $mVdec^{-1}$) compared to the crystalline CoP (73 $mVdec^{-1}$), but lower overpotential (see Fig. S24). Both prepared materials significantly showed lower Tafel slopes compared to the IrO_2/FTO (260 $mVdec^{-1}$).

Comparison of prepared materials activity for HER to other materials

Table S9 The activity of prepared materials as compared with other non-noble transition metal-based catalysts at 1 M KOH for HER.

Catalyst	Current density ($mAcm^{-2}$)	Overpotential η (mV)	Reference
Amorphous CoP/NF	**-10**	**143**	**This work**
	-100	**195**	**This work**
Crystalline CoP/NF	**-10**	**261**	**This work**
	-100	**334**	**This work**
$Ni_{11}(HPO_3)_8(OH)_6$/NF	-10	121	[11]
Fe-Ni-P hybrid catalyst	-10	14	[26]
CoN_x	-10	170	[41]
$NiCo_2P_x$ nanowires	-10	58	[42]
$Ni_{1-x}Co_xSe$ nanosheet	-10	85	[43]
FeP nanowire arrays	-10	194	[44]
Ni_5P_4 (pellet)	-10	49	[45]
$MoNi_4$ /MoO_2 cuboids	-10	15	[46]

Table S10 The activity of prepared materials as compared with other non-noble transition metal phosphide-based catalysts at 1 M KOH for HER.

Catalyst	Current density ($mAcm^{-2}$)	Overpotential η (mV)	Reference
Amorphous CoP/NF	**-10**	**143**	**This work**
	-100	**195**	**This work**
Crystalline CoP/NF	**-10**	**261**	**This work**
	-100	**334**	**This work**
Ni_5P_4 film	-10	180	[10]
Ni_xP_y-325	-20	160	[23]
Ni-P electrodeposited	-10	93	[24]
Ni_2P/GC	-10	220	[37]
MoP/Ni_2P/NF	-10	75	[47]
Ni_2P	-10	87	[48]
Ni_2P/NF	-10	85	[49]
$Ni_{12}P_5$/NF	-10	170	[49]
Ni_2P/GC	-20	250	[50]
Ni_2P/GC	-20	250	[51]

Table S11 The activity of prepared materials as compared with other cobalt phosphide-based catalysts at 1 M KOH for HER.

Catalyst	Current density ($mAcm^{-2}$)	Overpotential η (mV)	Reference
Amorphous CoP/NF	**-10**	**143**	**This work**
	-100	**195**	**This work**
Crystalline CoP/NF	**-10**	**261**	**This work**
	-100	**334**	**This work**
Amorphous CoP/FTO	**-10**	**228**	**This work**
	-100	**324**	**This work**
Crystalline CoP/FTO	**-10**	**377**	**This work**
	-100	**--**	**This work**
IrO_2/NF	**-10**	**209**	**This work**
	-100	**335**	**This work**
IrO_2/FTO	**-10**	**430**	**This work**
	-100	**--**	**This work**
Pt	**-10**	**39**	**This work**
	-100	**135**	**This work**
Cobalt-rich cobalt phosphide catalysts	-10	157	[29]
Nanostructured cobalt phosphide-based films	-10	196	[30]
Porous Cobalt Phosphide Polyhedrons	-10	116	[31]
CoP nanowire on Ti mesh	-10	72	[33]
CoP hollow polyhedron	-10	159	[34]
Co-P/NC nano-Polyhedrons	-10	154	[36]
Cobalt-phosphorus derived films/Cu	-10	94	[37]
Co_2P films/Co	-10	174	[52]
urchin-like cobalt phosphide microspheres film/TiO_2	-10	60	[53]
CoP/CC	-10	209	[54]
Co-P based nanoneedles	-10	95	[55]

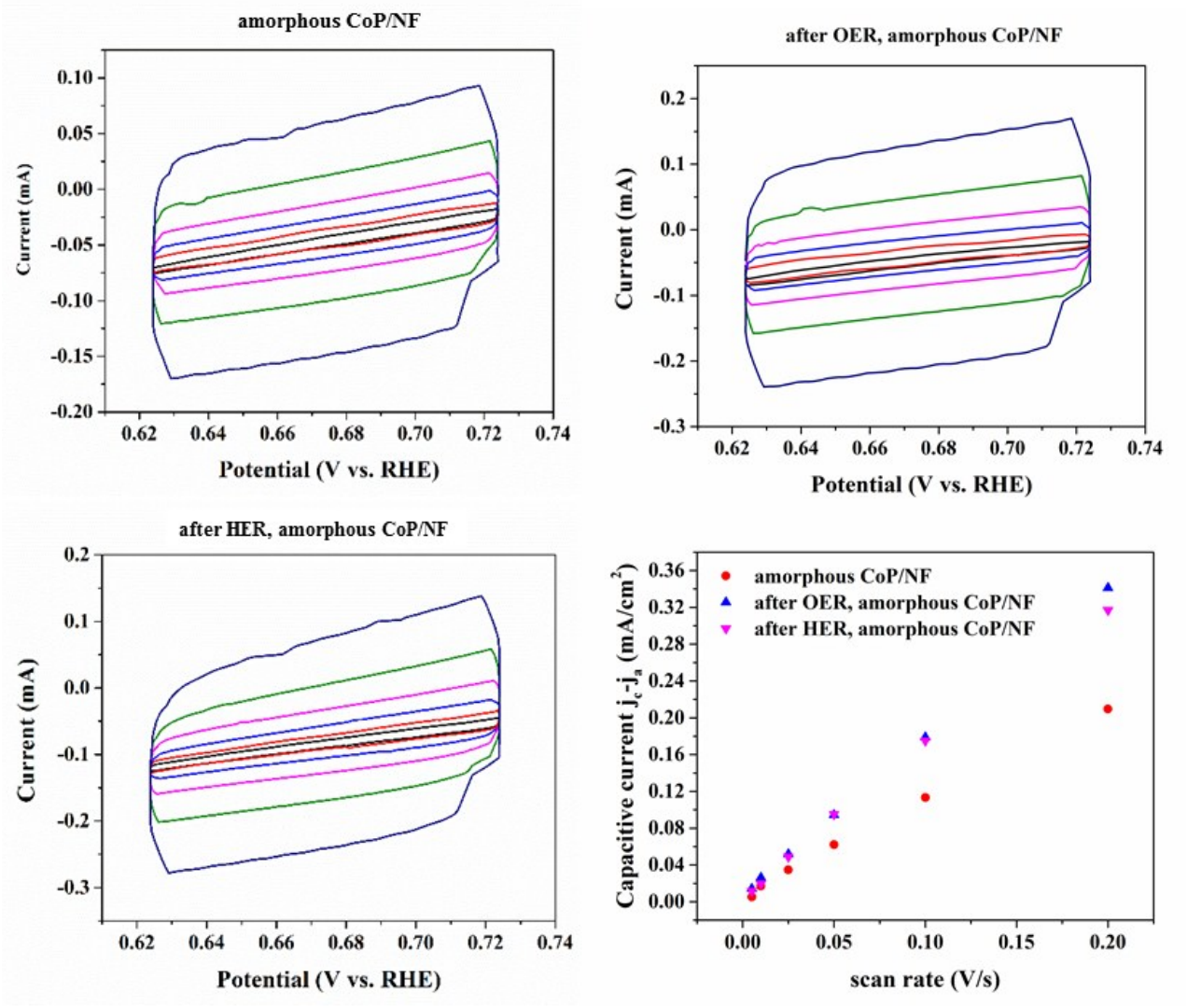

Fig. S26 The CV of amorphous CoP/NF (top left), after OER (top right) and after HER (bottom left) at a non-faradaic process region at different scan rates. Scan rates: 5 mVs^{-1} (black), 10 mVs^{-1} (red), 25 mVs^{-1} (blue), 50 mVs^{-1} (fuchsia), 100 mVs^{-1} (green), 200 mVs^{-1} (dark blue). The double layer capacitance (C_{DL}) was determined as the half of the slope from the plot of the capacitive current vs. scan rate plot (bottom right).

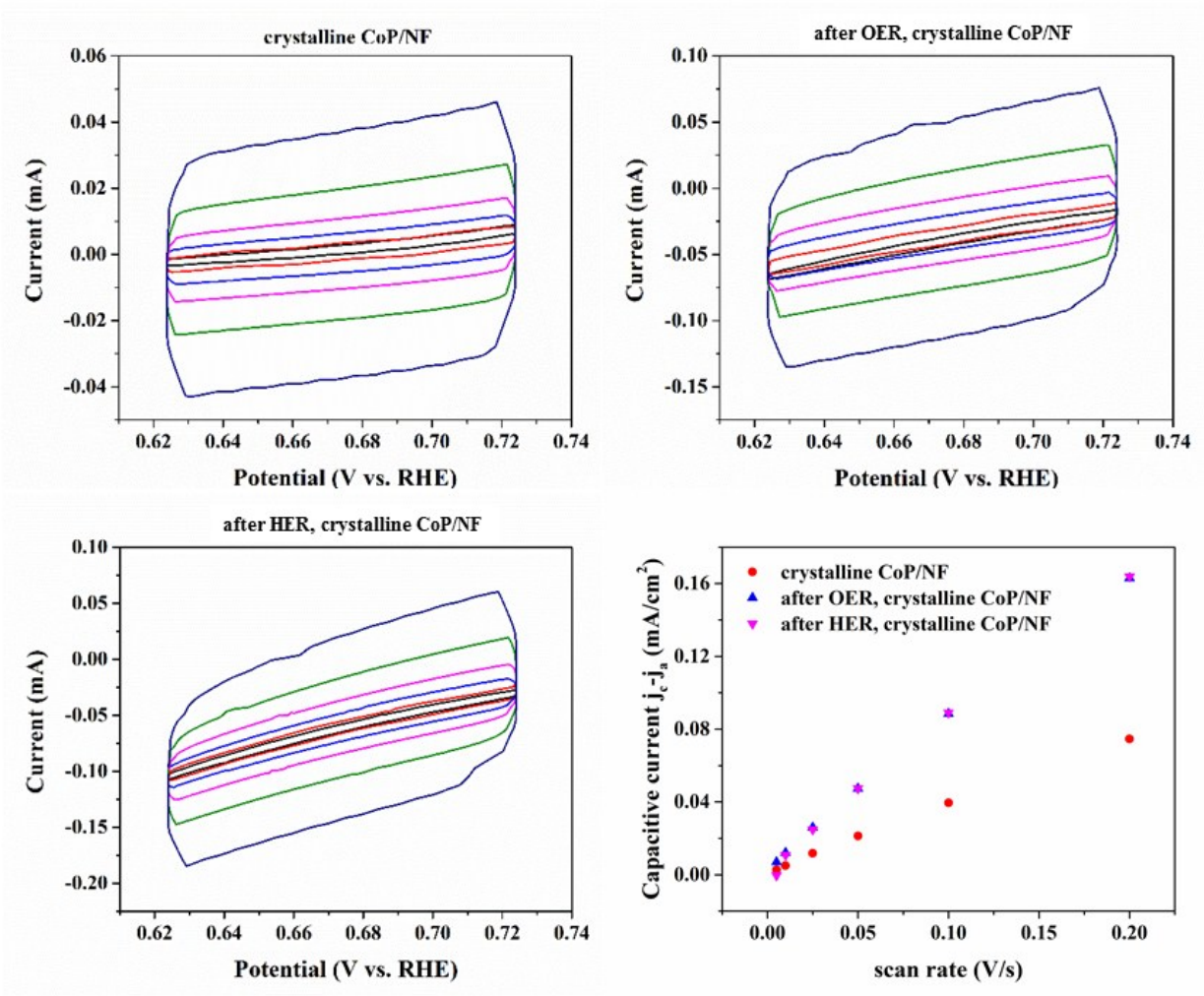

Fig. S27 The CV of crystalline CoP/NF (top left), after OER (top right) and after HER (bottom left) at a non-faradaic process region at different scan rates. Scan rates: 5 mVs^{-1} (black), 10 mVs^{-1} (red), 25 mVs^{-1} (blue), 50 mVs^{-1} (fuchsia), 100 mVs^{-1} (green), 200 mVs^{-1} (dark blue). The double layer capacitance was determined as the half of the slope from the plot of the capacitive current vs. scan rate plot (bottom right).

Table S12 Correlation factor (R^2) of the linear plot of capacitive current vs. scan rate, double layer capacitance (C_{DL}), calculated ECSA of the prepared materials over NF.

Material	R^2	C_{DL} (mF)	ECSA (cm^2)
amorphous CoP/NF	0.9985	0.5143	0.30
crystalline CoP/NF	0.9995	0.1833	0.11
OER amorphous CoP/NF	0.9998	0.8341	0.49
HER amorphous CoP/NF	0.9984	0.7842	0.46
OER crystalline CoP/NF	0.9992	0.3990	0.23
HER crystalline CoP/NF	0.9975	0.4115	0.24

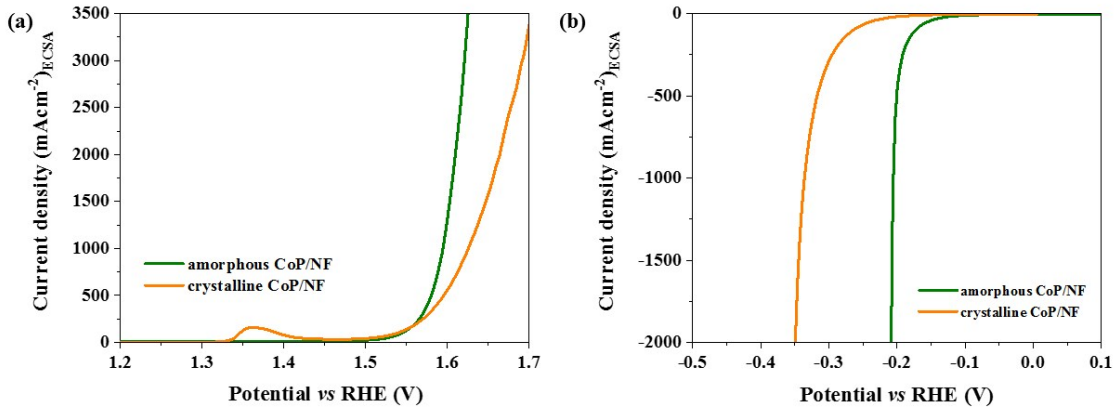

Fig. S28 Polarization curves of (a) OER and (b) HER of different CoP materials corrected by ECSA.

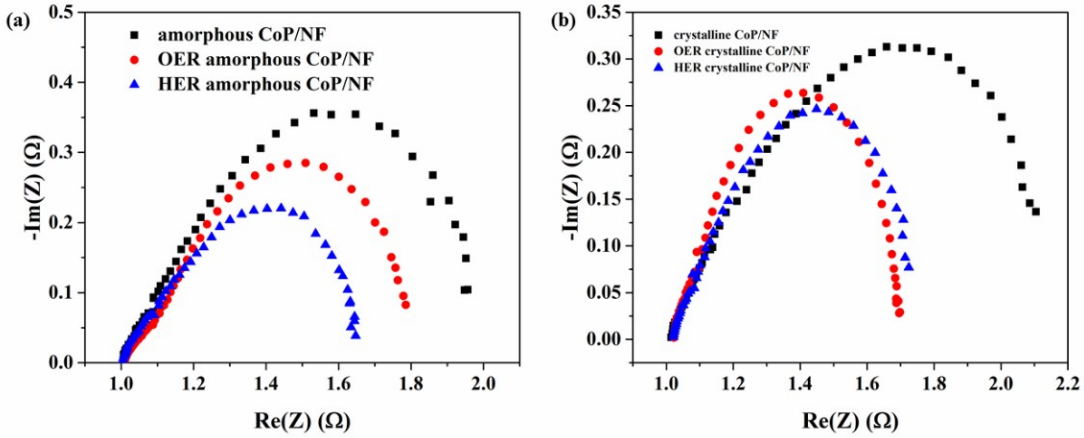

Fig. S29 Nyquist plot of a non-Faradaic region measured between 100 mHz and 100 kHz of (a) the amorphous CoP/NF (left) and (b) crystalline CoP/NF (right) compared to the materials after the OER and HER. The applied potential was 0.7 V vs Hg/HgO. From the fitting of data to semi-circle plots, it is possible to calculate the resistance of the solution (R_S) and the charge transfer resistance (R_{CT}).

Table S13 Charge transfer resistance (R_{CT}) and solution resistance (R_S) of the prepared materials over NF obtained from the Nyquist plot during the EIS experiments.

Material	R_{CT} (Ω)	R_S (Ω)
amorphous CoP/NF	0.8721	1.021
crystalline CoP/NF	1.0357	1.006
OER amorphous CoP/NF	0.6701	1.023
HER amorphous CoP/NF	0.6107	1.015
OER crystalline CoP/NF	0.6787	1.009
HER crystalline CoP/NF	0.5241	1.005

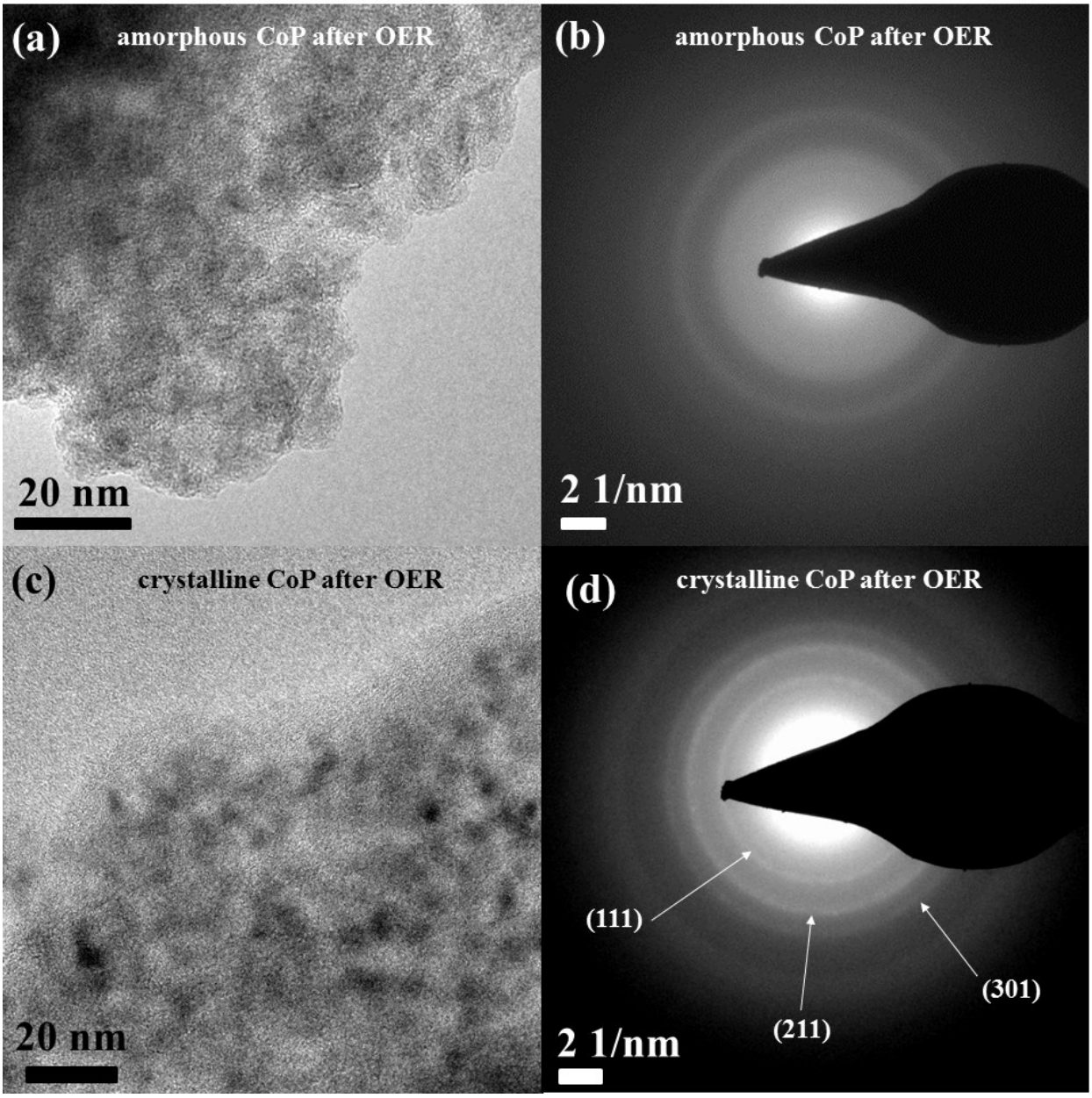

Fig. S30 (a) TEM and (b) SAED after OER of amorphous CoP, (c) TEM and (d) SAED after OER of crystalline CoP. No diffraction rings appear in the SAED on the amorphous material. In the case of the crystalline CoP, an amorphous layer is covering the agglomerated particles. However, small crystalline particles were also apparent, as confirmed by SAED pattern that is in accordance with CoP phase (JCPDS 29-0497).

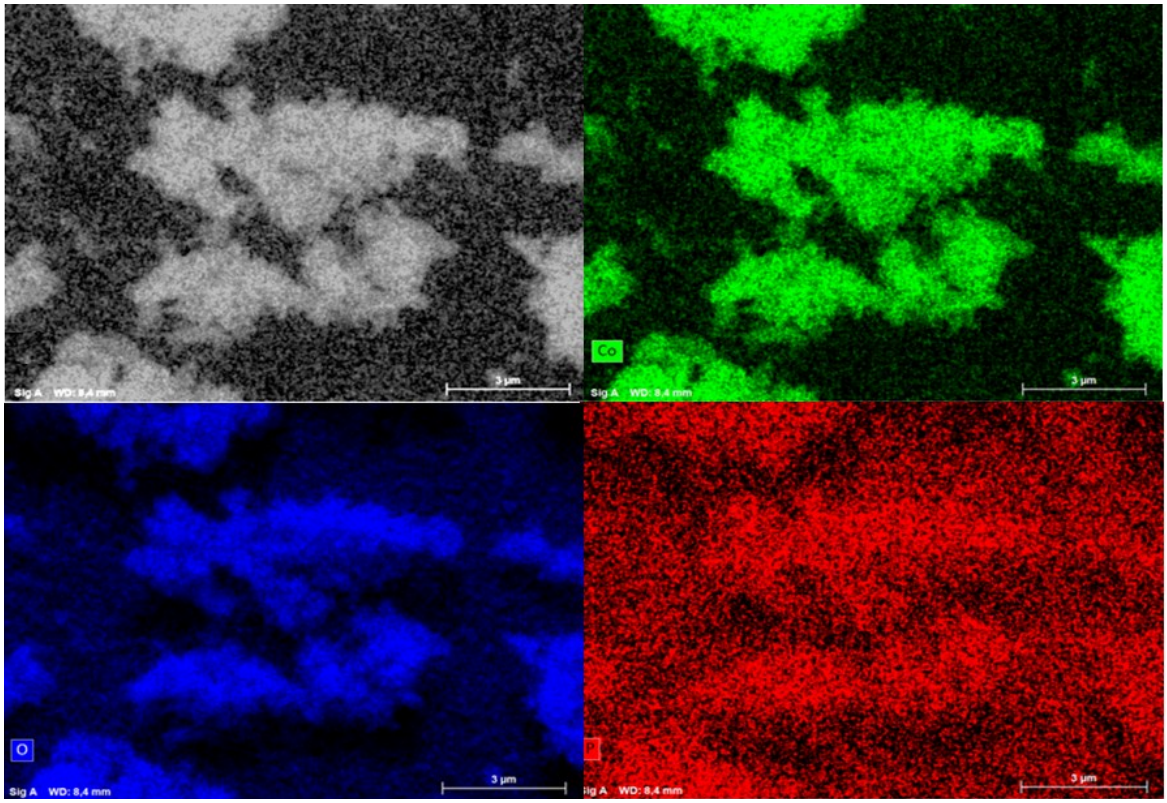

Fig. S31 Elemental mapping of amorphous CoP after OER. Elements: Co (green, left), P (red, centre), O (blue, right). Presence of Co and O along with a slight amount of P was observed. Oxygen is also present on the substrate (Si wafer). The figure shows a scale bar equivalent to 3 µm.

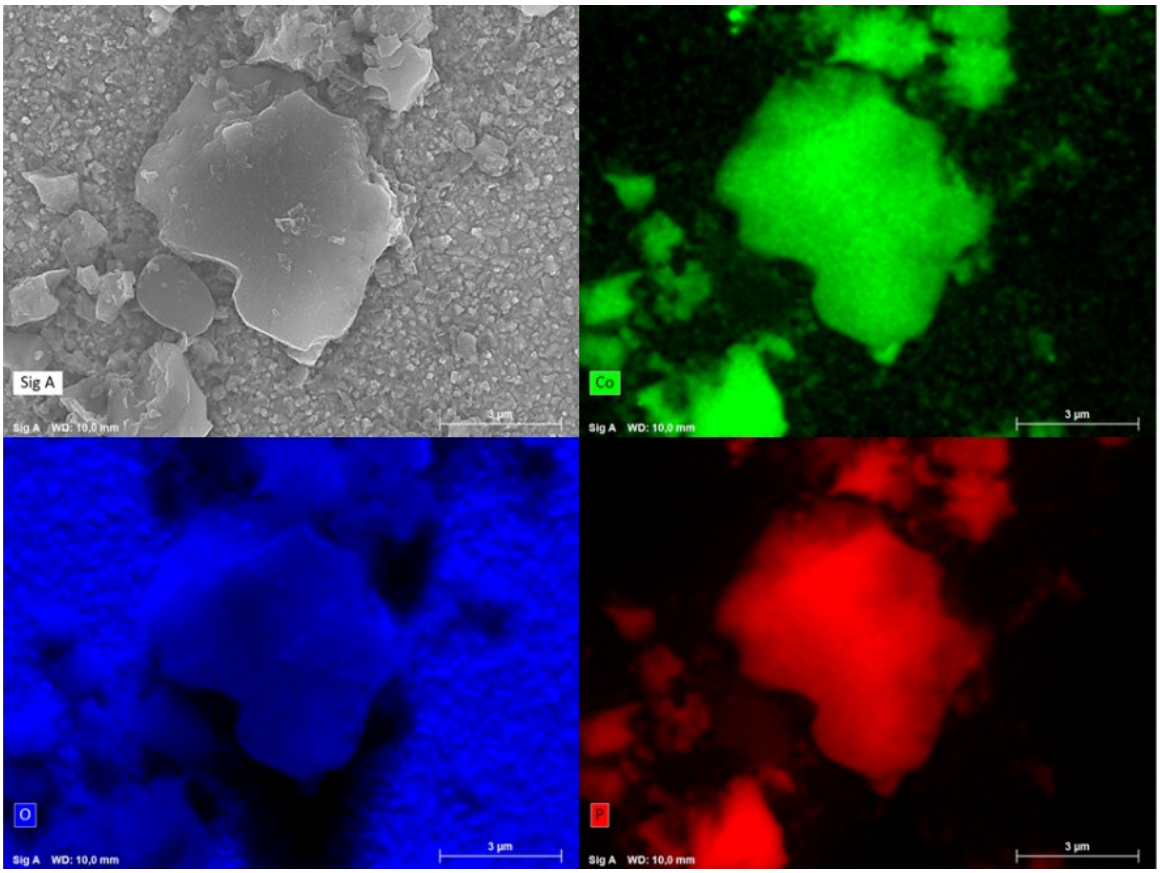

Fig. S32 Elemental mapping of crystalline CoP after OER. Elements: Co (green, top right), P (red, bottom right), O (blue, bottom left). Presence of the Co and O along with P in materials particle was observed. Oxygen is also present on the substrate (Si wafer). The figure shows a scale bar equivalent to 3 µm.

Table S14 The concentration of Co and P in the electrolyte solution after CP OER and CP HER experiments. The concentration was determined by ICP-AES of the solution. 2.5 mL of solution were dissolved to make up a 15 mL solution for the measurement. The percentage of element loss in solution was calculated from the concentration in solution, the Co:P ratio and the quantity of material involved in catalysis (0.4 mg). Phosphorus concentration in solution increases because of the high solubility of the generated polyphosphate species in the electrolyte.[56,57] Only a small amount of Co leaches into the solution, which could be explained by the difference in solubility of the oxidized cobalt species in the alkaline electrolyte, which is lower in comparison to the P-containing species.[58]

Sample	Co (mg/L)	P (mg/L)	% of element loss in solution	
			%Co	%P
1 M KOH	0.00	0.00	-	-
Amorphous CoP after OER CP	0.21	5.87	2%	85%
Amorphous CoP after HER CP	0.15	0.89	1%	13%
Crystalline CoP after OER CP	0.18	0.84	1%	11%
Crystalline CoP after HER CP	0.42	0.36	3%	5%

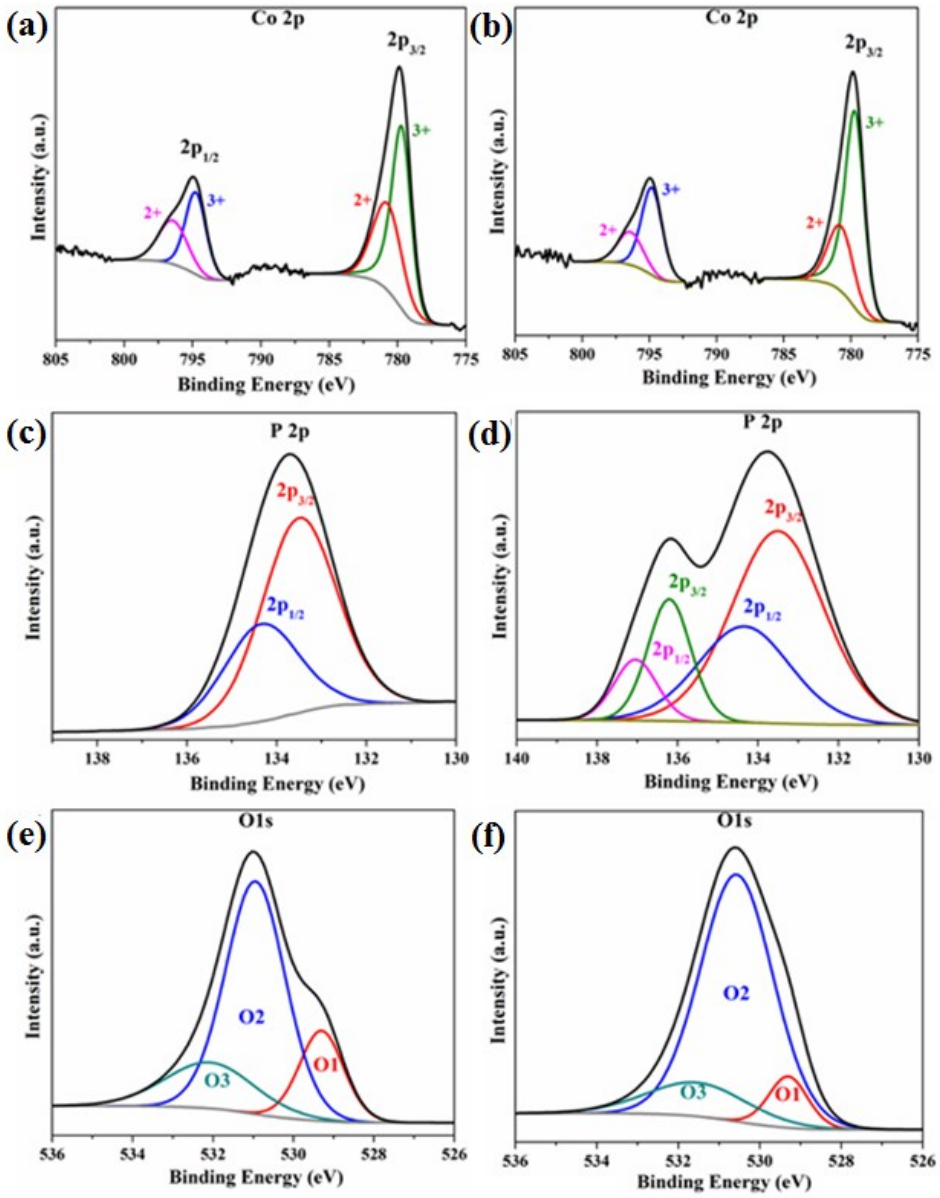

Fig. S33 The Co 2p, P 2p and O 1s XPS spectra of amorphous CoP after OER LSV (a, c and e) and OER CP (b, d and f). In both cases, total disappearance of the peaks associated to $Co^{\delta+}$ in CoP (778.7 eV in $2p_{3/2}$ and 793.9 eV and $2p_{1/2}$)[5] was observed with additional strong peaks corresponding to Co^{2+}/Co^{3+}. The deconvolution spectra of Co 2p displayed the enhancement of Co^{3+} peak area after CP compared to the Co^{2+} peak area suggesting a greater amount of Co oxidation under continuous OER. Similarly, after both LSV and CP experiments, $P^{\delta-}$ (peak at 129.0 eV) completely disappears and the oxidized P^{5+} (133.7 eV) peak appears.[3,7] Moreover, after CP OER, the peak centered at ~136.2 eV corresponding to P_2O_5 was also evolved.[59] The O 1s spectra shows three peaks (O1, O2 and O3) that can be correlated to the metal-oxygen bond in metal oxide (O1),[60] oxygen in –OH groups, indicating that the surface of the material is hydroxylated (O2),[61] and the absorbed water molecules on the materials (O3),[61] respectively.

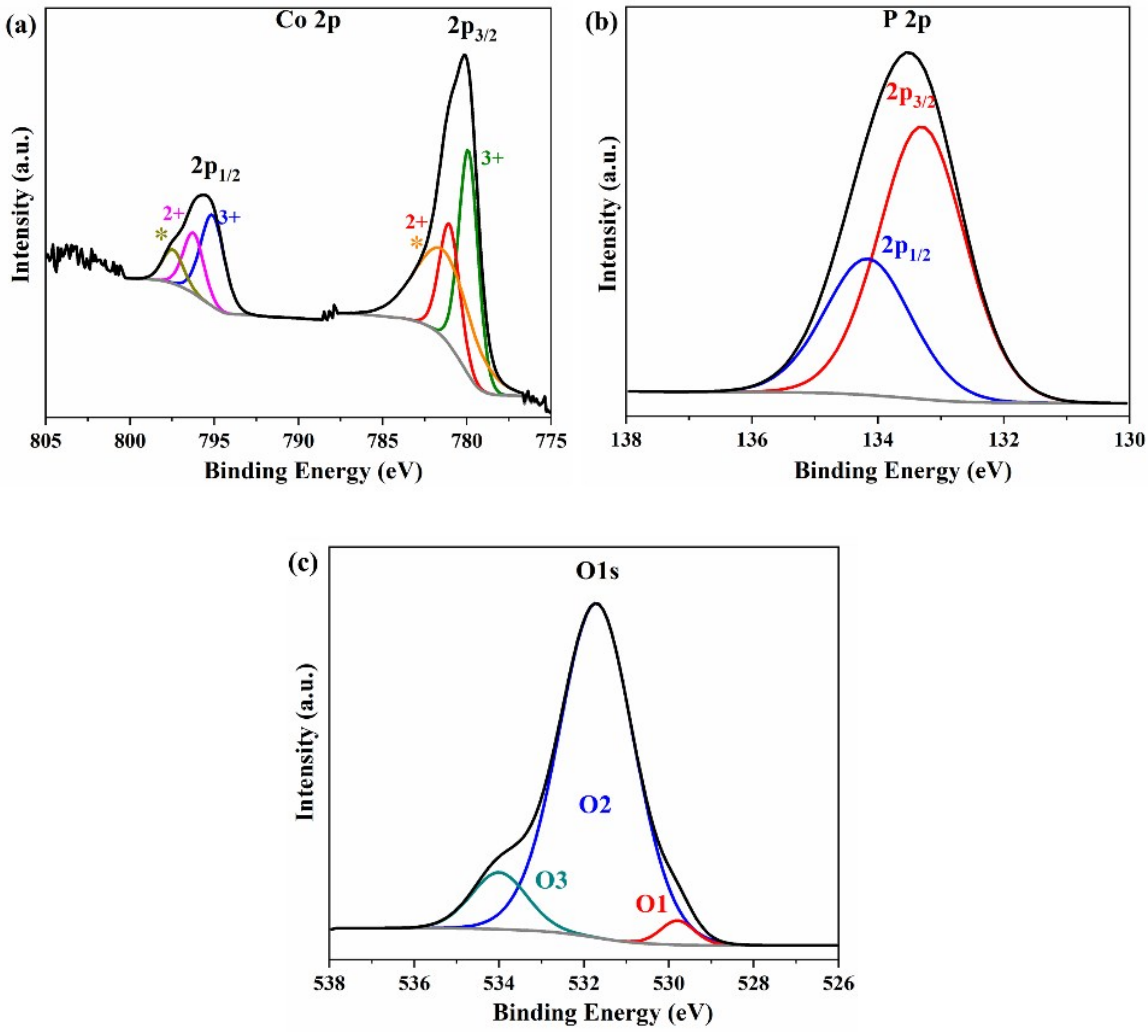

Fig. S34 The Co 2p, P 2p and O 1s XPS spectra of crystalline CoP after OER CP (a, b, c). After OER, the peak of Co^{3+} (deconvoluted: 795.2 eV, 780.0 eV)[5] increases its intensity in comparison to the Co^{2+} peak (deconvoluted: 796.3 eV, 781.1 eV).[5] After CP OER, only oxidized species P^{5+} (133.5 eV)[3,7] peak is observed. The reduced $P^{\delta-}$ peak (129.4eV, see Fig. S18) disappears. The O 1s spectra shows three peaks (O1, O2 and O3) that can be correlated to the metal-oxygen bond in metal oxide (O1), [60] oxygen in –OH groups, indicating that the surface of the material is hydroxylated (O2), [61] and the absorbed water molecules on the materials (O3),[61] respectively.

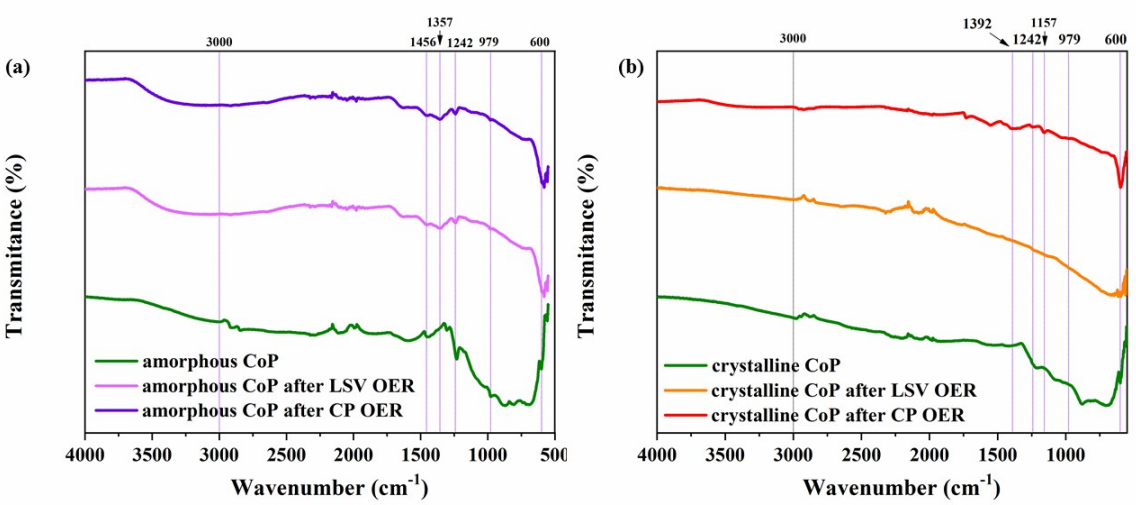

Fig. S35 Comparison of FTIR spectra of the materials after LSV and CP OER catalysis of amorphous and crystalline CoP. A broad band centered at ca. 3000 cm^{-1} appears on the spectra of the amorphous material and corresponds to adsorbed H_2O or possibly from the formed oxy(hydroxide) layer after surface oxidation. The small bands between 1500 cm^{-1} and 500 cm^{-1} are attributed to P=O stretching vibration and P-O-P stretching vibration on the phosphate groups.[3,4] The peak at 600 cm^{-1} is characteristic of Co-O bond.[4]

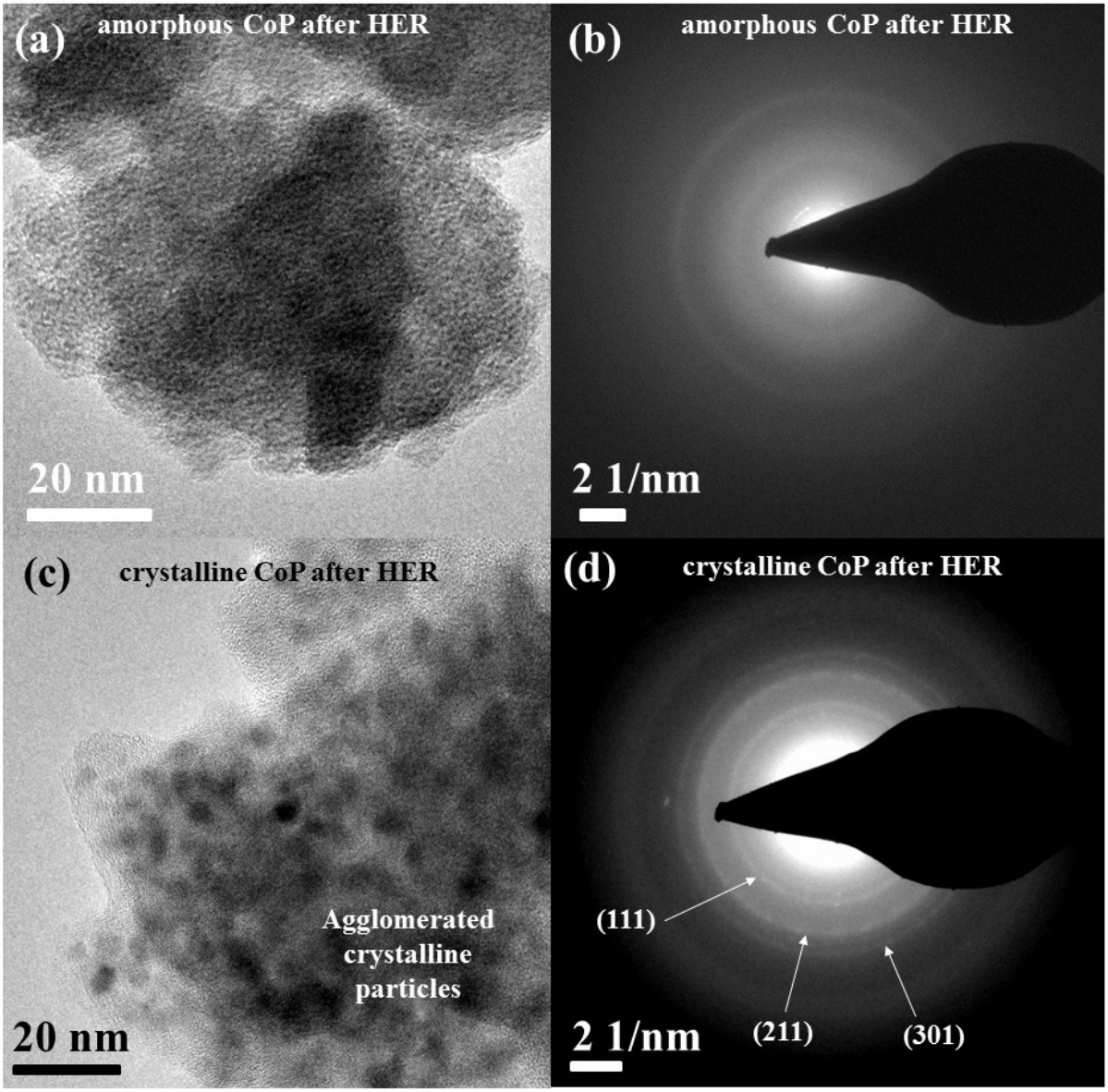

Fig. S36 (a) TEM and (b) SAED after HER of amorphous CoP. No diffraction rings appear in the SAED after OER, indicating that the material is still amorphous (see Fig. 1). (c) TEM and (d) SAED after HER of crystalline CoP. An amorphous layer is formed on the exterior of the particles. The inner part contained crystalline particles, as confirmed by SAED pattern (JCPDS 29-0497).

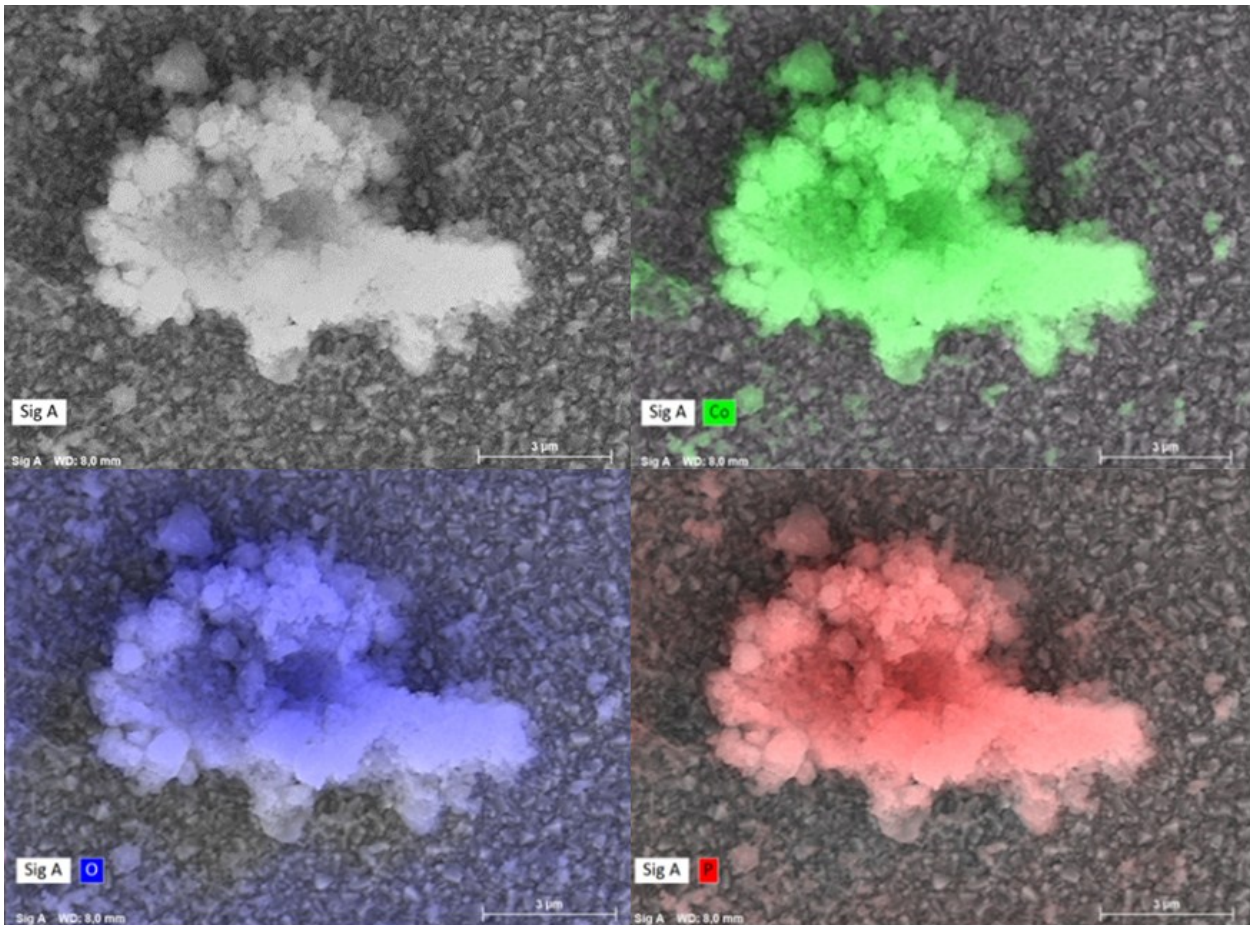

Fig. S37 Elemental mapping of amorphous CoP after HER. Elements: Co (green, top right), P (red, bottom right), O (blue, bottom, left). Presence of Co, O and P is observed from the images. O signals also come from the substrate (FTO). The figure shows a scale bar equivalent to 3 μm.

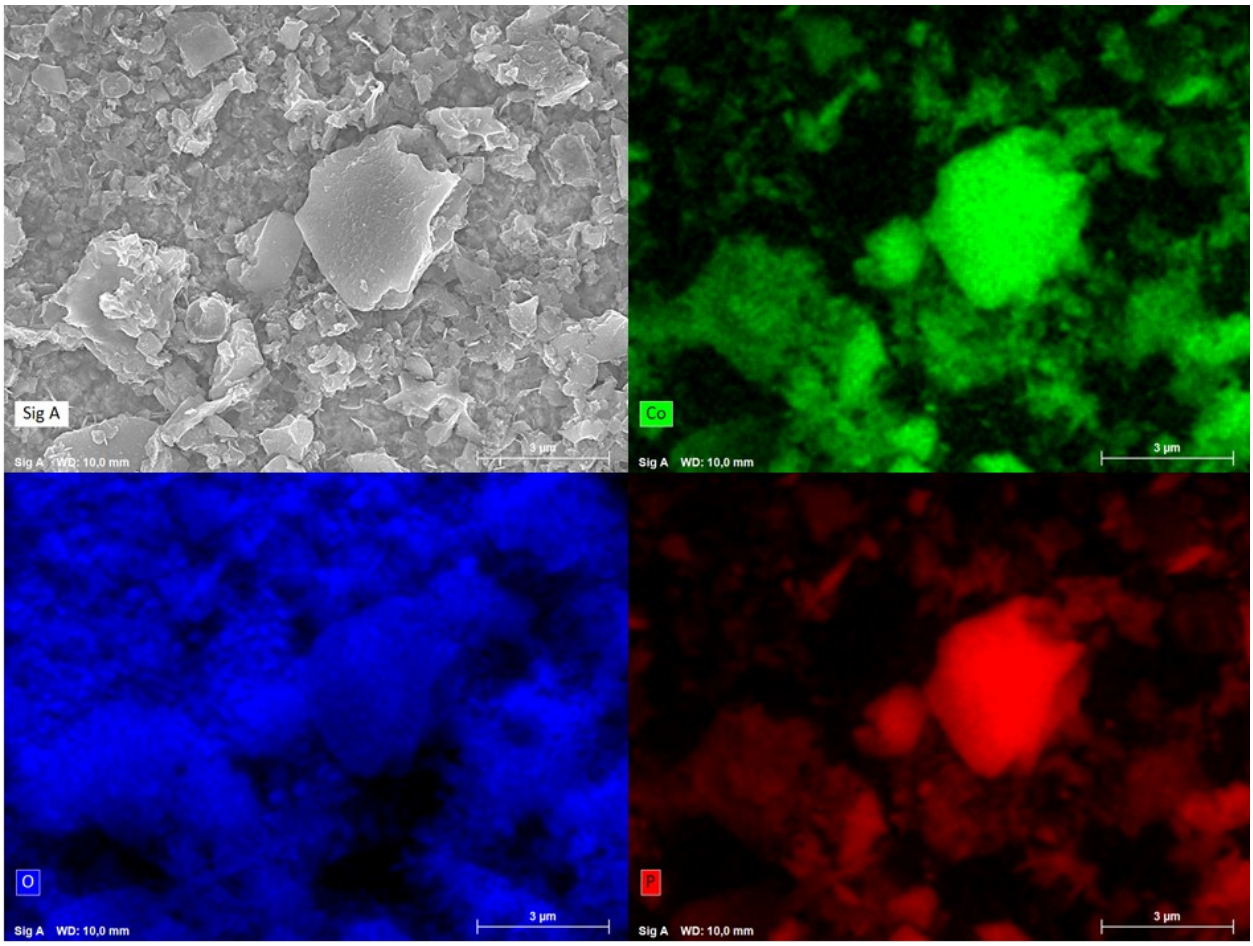

Fig. S38 Elemental mapping of crystalline CoP after HER. Elements: Co (green, top right), P (red, bottom right), O (blue, bottom left). Presence of Co, O and P is observed from the images. O signals also come from the substrate (FTO). The figure shows a scale bar equivalent to 3 µm.

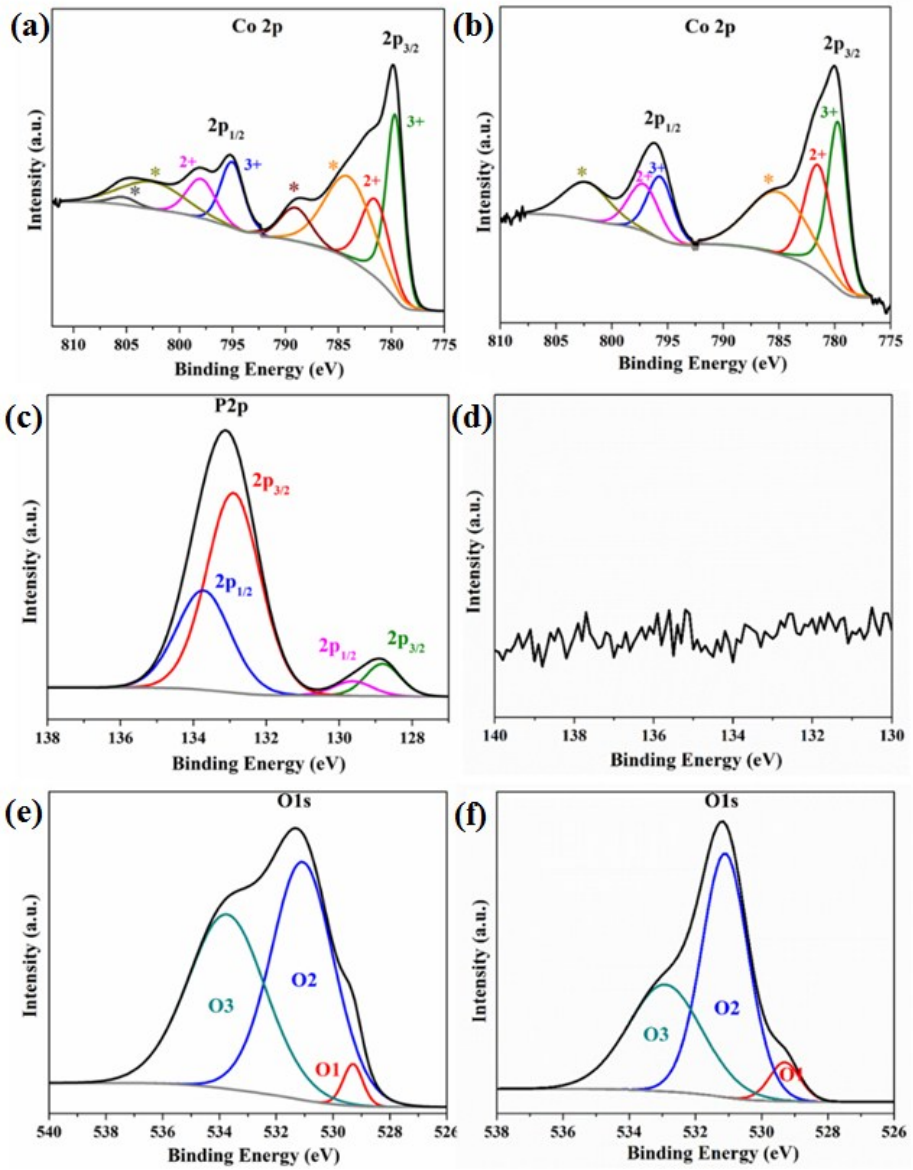

Fig. S39 The Co 2p, P 2p and O 1s XPS spectra of amorphous CoP after HER LSV (a, c and e) and HER CP (b, d, f) for amorphous CoP. In the Co 2p spectra, similar peaks were obtained in both cases, with a total disappearance peaks associated to of the $Co^{\delta+}$ and appearance of peaks for Co^{2+} and Co^{3+} which is due to the surface passivation under strongly alkaline conditions.[3] The peak of $P^{\delta-}$ (129.0 eV) in the spectra after LSV HER has a reduced intensity if compared to the initial spectrum (Fig. 2 on manuscript), with the most intense peak corresponding to P^{5+} (133.1 eV).[3,7] In the case of the spectrum after CP, the peaks for P was completely disappeared further demonstrating the loss of P in HER conditions that match with ICP-AES results (Table S14). The O 1s spectrum for LSV and CP showed three distinct peaks (O1, O2 and O3) corresponding to the metal-oxygen bond in metal oxide (O1),[60] oxygen in –OH groups, indicating that the surface of the material is hydroxylated (O2),[61] and the absorbed water molecules on the materials (O3),[61] respectively.

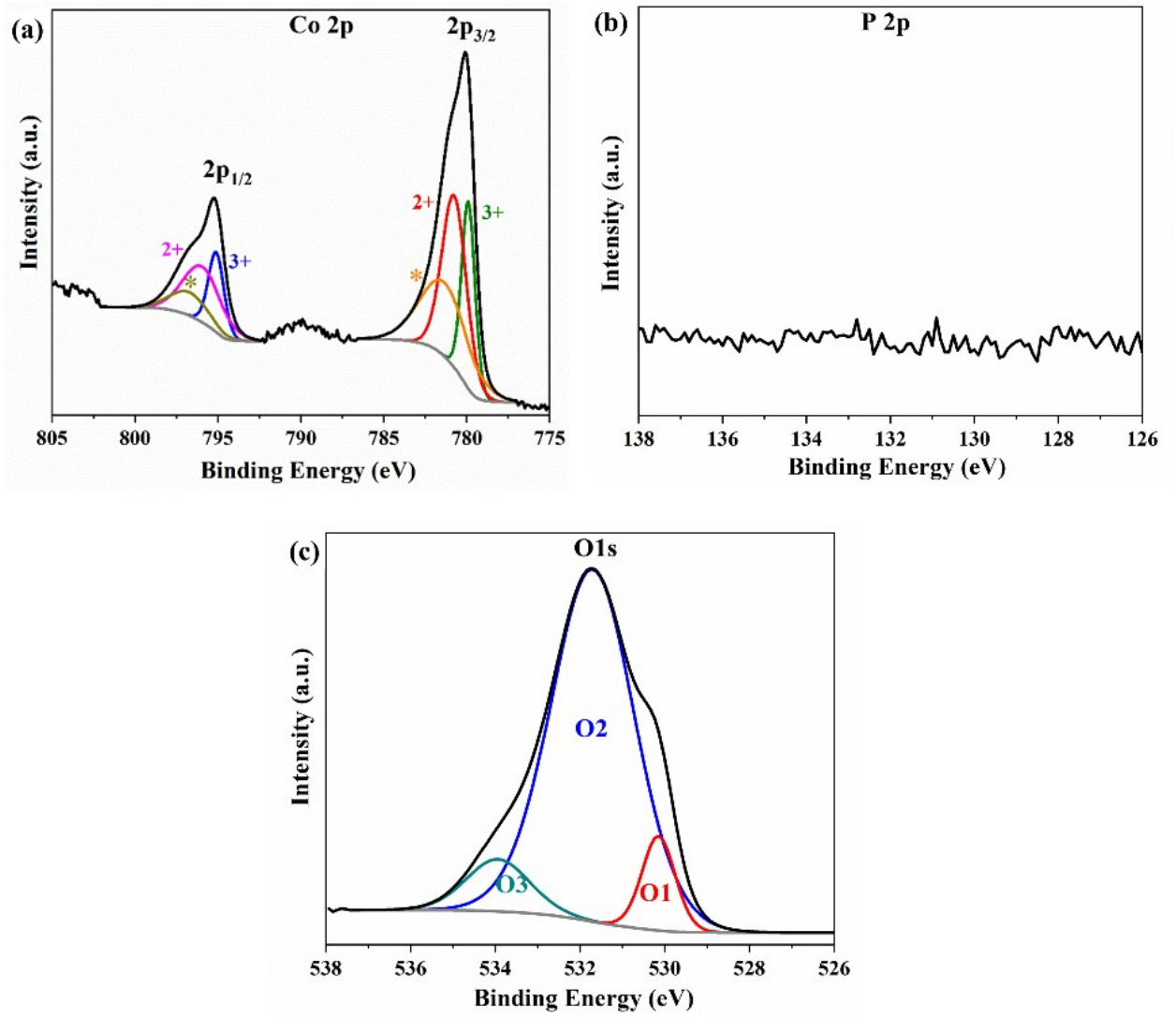

Fig. S40 XPS of Co, P and O after HER CP (a, b, c, respectively) for crystalline CoP. The Co 2p, P 2p and O1s spectra could be described similar to Fig. S39.

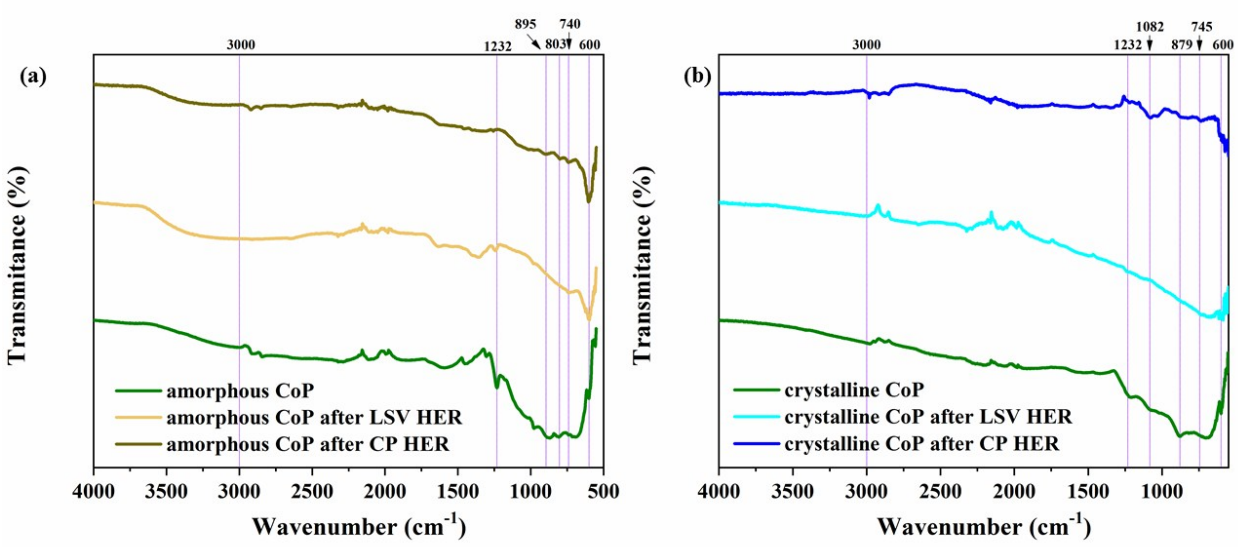

Fig. S41 Comparison of FTIR of the obtained materials after LSV and CP HER catalysis of amorphous and crystalline CoP. A broad band centered at ca. 3000 cm^{-1} appears in the spectra of the amorphous material and corresponds to adsorbed H_2O or possibly from the formed oxy(hydroxide) layer after surface oxidation. The broad lower transmittance range between 1250 cm^{-1} and 500 cm^{-1}, where peaks associated to phosphate groups appear,[3,4] shows no intense peaks indicating a loss of phosphate.

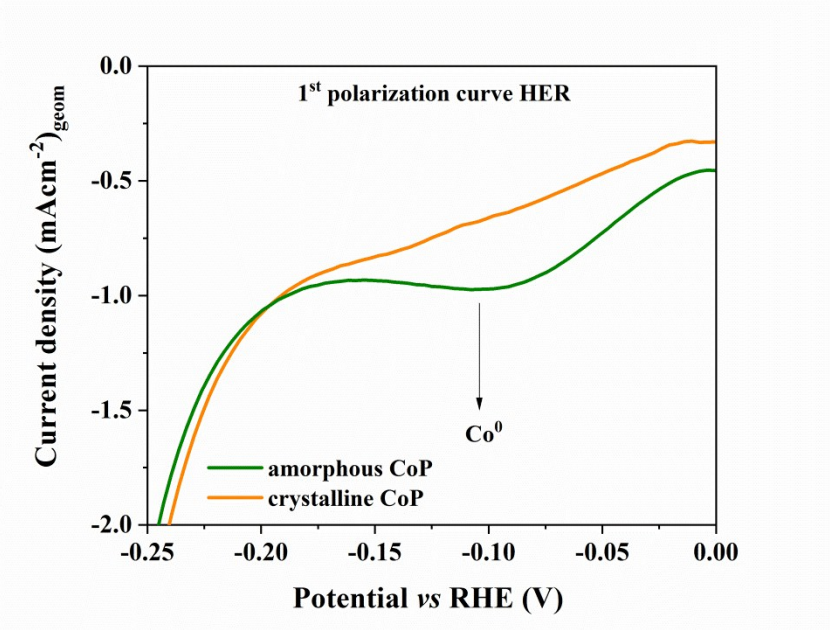

Fig. S42 Initial polarization curve of amorphous and crystalline CoP measured in 1 M KOH on NF with a sweep rate 10 mVs^{-1} featuring a cathodic peak corresponding to the reduction of higher valent cobalt species to metallic cobalt.

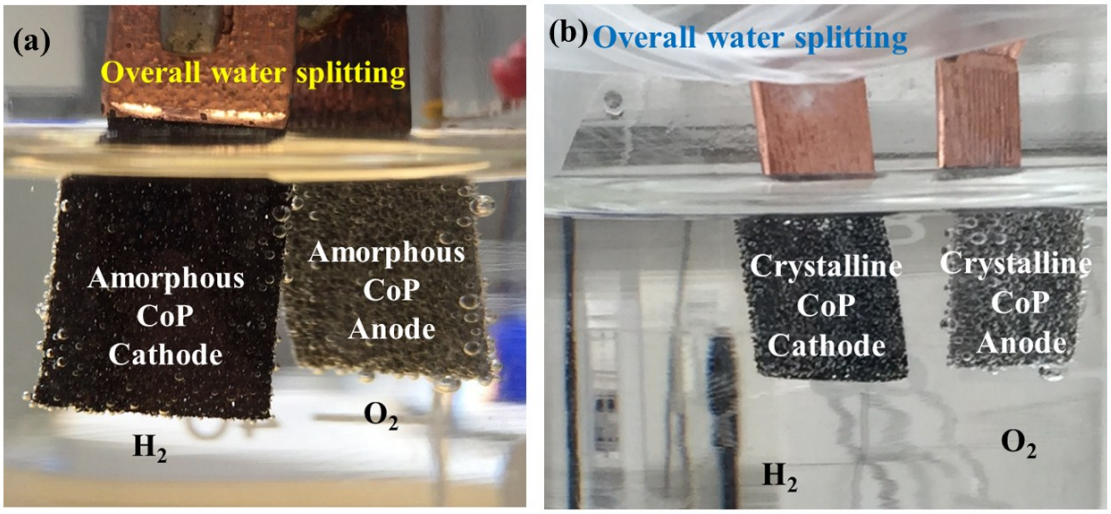

Fig. S43 Overall water-splitting with (a) amorphous and (b) crystalline CoP on a CoP/NF ‖ CoP/NF two-electrode system in 1 M KOH solution. Vigorous bubble formation on the cathode and anode was observed during the experiment.

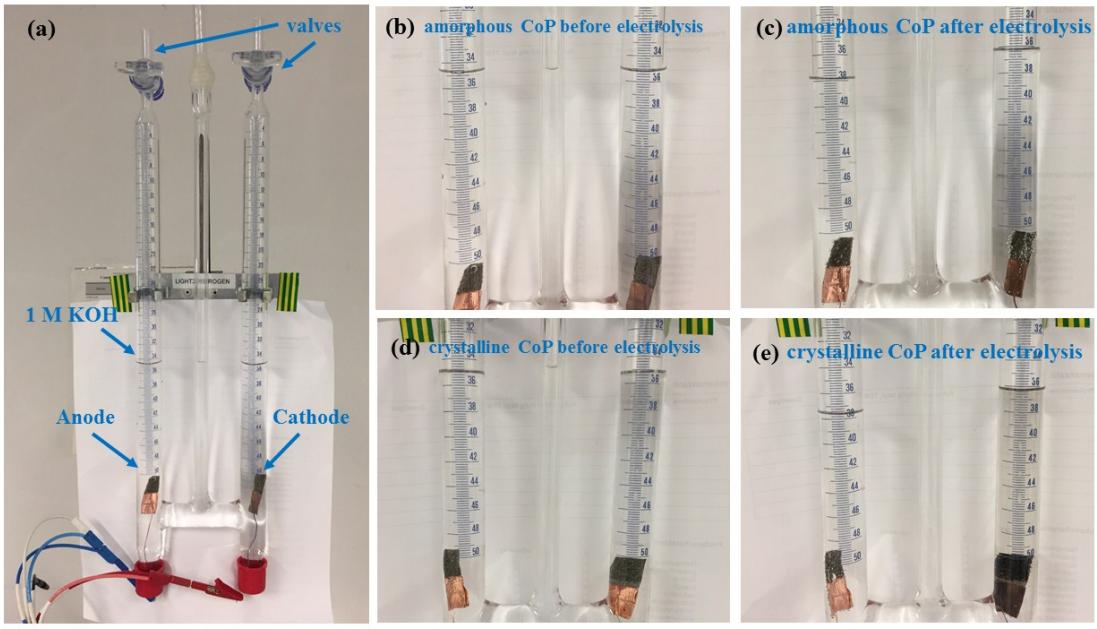

Fig. S 44 a) In inverted two-electrode amorphous CoP ‖ amorphous CoP electrolyser was used under constant current density of 10 $mAcm^{-2}$ in 1 M KOH to allow the collection of H_2 and O_2 separately at atmospheric pressure. b) The initial level of the electrolyte was noted and then the valves were closed. During electrolysis, because of evolution and collection of H_2 and O_2 at the upper part of the cell, the level of electrolyte goes down and the change in volume over time was noted. c) The ratio of volumes of H_2 and O_2 remained almost 2:1 over one hour of electrolysis. A similar system was built using a two-electrode crystalline CoP ‖ crystalline CoP electrolyser. (d and e).

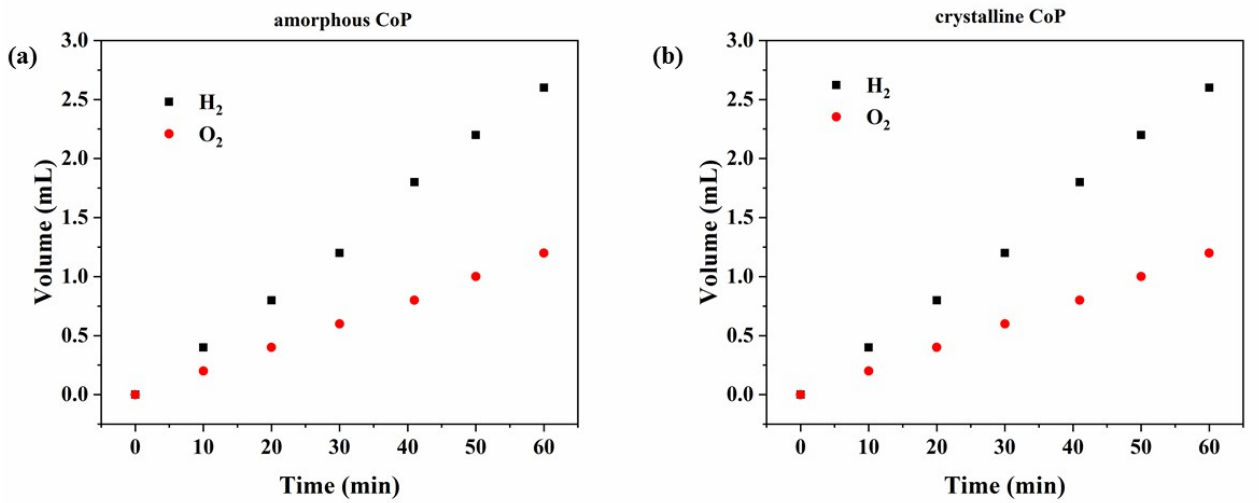

Fig. S 45 The plot of volume change as result of H_2 and O_2 evolution in the experiments respect to time for (a) amorphous CoP and (b) crystalline CoP. The ratios of H_2 and O_2 were obtained from the electrodes of both materials deposited on NF as both cathode and anode in 1 M KOH solution at a current of 10 mAcm^{-2} for 1 h. The attained ratios directly confirmed the evolution of gases as well as the amount of H_2 was approximately twice larger than the O_2 demonstrating the efficient selectivity and reactivity of the catalysts.

Calculation of Faradaic efficiency

The Faradaic efficiency (FE) of the materials in 1M KOH towards oxygen and hydrogen evolution reaction was measured in a two-electrode configuration where nickel foam loaded with the catalysts were used as both cathode and anode in a closed electrochemical cell. The electrolyte and cell were first degassed with Argon for 30 min under stirring. Afterwards, constant current density of 10 mAcm^{-2} was applied for a certain period. At the end of electrolysis, the gaseous samples were drawn from the headspace by a gas tight syringe and analysed by a GC calibrated for H_2, and O_2. Each injection was repeated at least three times and the average value is presented.

The Faradaic efficiency (FE) is calculated based on:

$$FE(H_2,\%) = \frac{V_{H_2} \times 2 \times F}{V_m \times j \times t} \times 100\%$$

$$FE(O_2,\%) = \frac{V_{O_2} \times 4 \times F}{V_m \times j \times t} \times 100\%$$

V_{H_2}, V_{O_2} is the evolved volume of hydrogen and oxygen, F is the Faraday constant (96485.33289 C/mol), V_m is the molar volume of the gas, j is the current density (10 mAcm^{-2}) and t is the time of electrolysis.

Table S15 Calculation of Faradaic efficiency for amorphous CoP

	j (mAcm^{-2})	**t (s)**	V_{H_2} **(mL)**	V_{O_2} **(mL)**	V_{H_2}**:** V_{O_2}	**FE (H_2, %)**	**FE (O_2, %)**
Amorphous CoP	10	400	0.44	0.21	2.07	96%	92%

References

1 S. Yao, N. Lindenmaier, Y. Xiong, S. Inoue, T. Szilvási, M. Adelhardt, J. Sutter, K. Meyer and M. Driess, *Angew. Chemie Int. Ed.*, 2015, **54**, 1250–1254.

2 R. J. Kern, *J. Inorg. Nucl. Chem.*, 1962, **24**, 1105–1109.

3 L. Ai, Z. Niu and J. Jiang, *Electrochim. Acta*, 2017, **242**, 355–363.

4 Y. Liu and D. G. Nocera, *J. Phys. Chem. C*, 2014, **118**, 17060–17066.

5 A. P. Grosvenor, S. D. Wik, R. G. Cavell and A. Mar, *Inorg. Chem.*, 2005, **44**, 8988–8998.

6 D. Liu, L. Jing, P. Luan, J. Tang and H. Fu, *ACS Appl. Mater. Interfaces*, 2013, **5**, 4046–4052.

7 J. Chang, Y. Xiao, M. Xiao, J. Ge, C. Liu and W. Xing, *ACS Catal.*, 2015, **5**, 6874–6878.

8 Q. Wang, L. Zhong, J. Sun and J. Shen, *Chem. Mater.*, 2005, **17**, 3563–3569.

9 H. Hu, B. Guan, B. Xia and X. W. (David) Lou, *J. Am. Chem. Soc.*, 2015, **137**, 5590–5595.

10 F. Song and X. Hu, *Nat. Commun.*, 2014, **5**, 4477.

11 P. W. Menezes, C. Panda, S. Loos, F. Bunschei-Bruns, C. Walter, M. Schwarze, X. Deng, H. Dau and M. Driess, *Energy Environ. Sci.*, 2018, **11**, 1287–1298.

12 M. W. Louie and A. T. Bell, *J. Am. Chem. Soc.*, 2013, **135**, 12329–12337.

13 B. Zhang, X. Zheng, O. Voznyy, R. Comin, M. Bajdich, M. Garcia-Melchor, L. Han, J. Xu, M. Liu, L. Zheng, F. P. Garcia de Arquer, C. T. Dinh, F. Fan, M. Yuan, E. Yassitepe, N. Chen, T. Regier, P. Liu, Y. Li, P. De Luna, A. Janmohamed, H. L. Xin, H. Yang, A. Vojvodic and E. H. Sargent, *Science*, 2016, **352**, 333–337.

14 J. A. Koza, Z. He, A. S. Miller and J. A. Switzer, *Chem. Mater.*, 2012, **24**, 3567–3573.

15 M. Al-Mamun, X. Su, H. Zhang, H. Yin, P. Liu, H. Yang, D. Wang, Z. Tang, Y. Wang and H. Zhao, *Small*, 2016, **12**, 2866–2871.

16 X. Long, J. Li, S. Xiao, K. Yan, Z. Wang, H. Chen and S. Yang, *Angew. Chemie - Int. Ed.*, 2014, **53**, 7584–7588.

17 T. Liu, Y. Liang, Q. Liu, X. Sun, Y. He and A. M. Asiri, *Electrochem. commun.*, 2015, **60**, 92–96.

18 C. Xia, Q. Jiang, C. Zhao, M. N. Hedhili and H. N. Alshareef, *Adv. Mater.*, 2016, **28**, 77–85.

19 J. Xu, J. Li, D. Xiong, B. Zhang, Y. Liu, K. H. Wu, I. Amorim, W. Li and L. Liu, *Chem. Sci.*, 2018, **9**, 3470–3476.

20 L.-A. Stern, L. Feng, F. Song and X. Hu, *Energy Environ. Sci.*, 2015, **8**, 2347–2351.

21 A. Han, H. Chen, Z. Sun, J. Xu and P. Du, *Chem. Commun.*, 2015, **51**, 11626–11629.

22 M. Ledendecker, S. Krick Calderón, C. Papp, H.-P. Steinrück, M. Antonietti and M. Shalom, *Angew. Chemie Int. Ed.*, 2015, **54**, 12361–12365.

23 N. Jiang, B. You, M. Sheng and Y. Sun, *ChemCatChem*, 2016, **8**, 106–112.

24 H. Liang, F. Meng, M. Cabán-Acevedo, L. Li, A. Forticaux, L. Xiu, Z. Wang and S. Jin, *Nano Lett.*, 2015, **15**, 1421–1427.

25 J. Masud, S. Umapathi, N. Ashokaan and M. Nath, *J. Mater. Chem. A*, 2016, **4**, 9750–9754.

26 F. Yu, H. Zhou, Y. Huang, J. Sun, F. Qin, J. Bao, W. A. Goddard, S. Chen and Z. Ren, *Nat. Commun.*, 2018, **9**, 1–9.

27 D. Li, H. Baydoun, C. N. Verani and S. L. Brock, *J. Am. Chem. Soc.*, 2016, **138**, 4006–4009.

28 M. Zhu, Y. Zhou, Y. Sun, C. Zhu, L. Hu, J. Gao, H. Huang, Y. Liu and Z. Kang, *Dalt. Trans.*, 2018, **47**, 5459–5464.

29 C.-Z. Yuan, S.-L. Zhong, Y.-F. Jiang, Z. K. Yang, Z.-W. Zhao, S.-J. Zhao, N. Jiang and A.-W. Xu, *J. Mater. Chem. A*, 2017, **5**, 10561–10566.

30 J. A. Vigil and T. N. Lambert, *RSC Adv.*, 2015, **5**, 105814–105819.

31 F. Li, Y. Bu, Z. Lv, J. Mahmood, G. F. Han, I. Ahmad, G. Kim, Q. Zhong and J. B. Baek, *Small*, 2017, **13**, 1–6.

32 S. Anantharaj, P. N. Reddy and S. Kundu, *Inorg. Chem.*, 2017, **56**, 1742–1756.

33 L. Ai, Z. Niu, J. Jiang, L. Yang, H. Qi, C. Zhang and X. Sun, *Nanotechnology*, 2016, **27**, 23LT01.

34 M. Liu and J. Li, *ACS Appl. Mater. Interfaces*, 2016, **8**, 2158–2165.

35 J. Masa, S. Barwe, C. Andronescu, I. Sinev, A. Ruff, K. Jayaramulu, K. Elumeeva, B. Konkena, B. Roldan Cuenya and W. Schuhmann, *ACS Energy Lett.*, 2016, **1**, 1192–1198.

36 B. You, N. Jiang, M. Sheng, S. Gul, J. Yano and Y. Sun, *Chem. Mater.*, 2015, **27**, 7636–7642.

37 N. Jiang, B. You, M. Sheng and Y. Sun, *Angew. Chemie Int. Ed.*, 2015, **54**, 6251–6254.

38 Y.-P. Zhu, Y.-P. Liu, T.-Z. Ren and Z.-Y. Yuan, *Adv. Funct. Mater.*, 2015, **25**, 7337–7347.

39 Y. Yang, H. Fei, G. Ruan and J. M. Tour, *Adv. Mater.*, 2015, **27**, 3175–3180.

40 Y.-C. Liu, J. A. Koza and J. A. Switzer, *Electrochim. Acta*, 2014, **140**, 359–365.

41 H.-W. Liang, S. Brüller, R. Dong, J. Zhang, X. Feng and K. Müllen, *Nat. Commun.*, 2015, **6**, 7992.

42 R. Zhang, X. Wang, S. Yu, T. Wen, X. Zhu, F. Yang, X. Sun, X. Wang and W. Hu, *Adv. Mater.*, 2017, **29**, 1605502.

43 B. Liu, Y.-F. Zhao, H.-Q. Peng, Z.-Y. Zhang, C.-K. Sit, M.-F. Yuen, T.-R. Zhang, C.-S. Lee and W.-J. Zhang, *Adv. Mater.*, 2017, **29**, 1606521–1606528.

44 C. Y. Son, I. H. Kwak, Y. R. Lim and J. Park, *Chem. Commun.*, 2016, **52**, 2819–2822.

45 A. B. Laursen, K. R. Patraju, M. J. Whitaker, M. Retuerto, T. Sarkar, N. Yao, K. V. Ramanujachary, M. Greenblatt and G. C. Dismukes, *Energy Environ. Sci.*, 2015, **8**, 1027–1034.

46 J. Zhang, T. Wang, P. Liu, Z. Liao, S. Liu, X. Zhuang, M. Chen, E. Zschech and X. Feng, *Nat. Commun.*, 2017, **8**, 1–8.

47 C. Du, M. Shang, J. Mao and W. Song, *J. Mater. Chem. A*, 2017, **5**, 15940–15949.

48 R. Zhang, P. A. Russo, M. Feist, P. Amsalem, N. Koch and N. Pinna, *ACS Appl. Mater. Interfaces*, 2017, **9**, 14013–14022.

49 P. W. Menezes, A. Indra, C. Das, C. Walter, C. Göbel, V. Gutkin, D. Schmeiβer and M. Driess, *ACS Catal.*, 2017, **7**, 103–109.

50 E. J. Popczun, J. R. McKone, C. G. Read, A. J. Biacchi, A. M. Wiltrout, N. S. Lewis and R. E. Schaak, *J. Am. Chem. Soc.*, 2013, **135**, 9267–9270.

51 L. Feng, H. Vrubel, M. Bensimon and X. Hu, *Phys. Chem. Chem. Phys.*, 2014, **16**, 5917–5921.

52 C. G. Read, J. F. Callejas, C. F. Holder and R. E. Schaak, *ACS Appl. Mater. Interfaces*, 2016, **8**, 12798–12803.

53 D. Zhou, L. He, W. Zhu, X. Hou, K. Wang, G. Du, C. Zheng, X. Sun and A. M. Asiri, *J. Mater. Chem. A*, 2016, **4**, 10114–10117.

54 J. Tian, Q. Liu, A. M. Asiri and X. Sun, *J. Am. Chem. Soc.*, 2014, **136**, 7587–7590.

55 P. Wang, F. Song, R. Amal, Y. H. Ng and X. Hu, *ChemSusChem*, 2016, **9**, 472–477.

56 Z. Wu, Q. Gan, X. Li, Y. Zhong and H. Wang, *J. Phys. Chem. C*, 2018, **122**, 2848–2853.

57 A. Indra, P. W. Menezes, N. R. Sahraie, A. Bergmann, C. Das, M. Tallarida, D. Schmeißer, P. Strasser and M. Driess, *J. Am. Chem. Soc.*, 2014, **136**, 17530–17536.

58 Y. Zhang, L. Gao, E. J. M. M. Hensen and J. P. Hofmann, *ACS Energy Lett.*, 2018, **3**, 1360–1365.

59 R. Gresch, W. Müller-Warmuth and H. Dutz, *J. Non. Cryst. Solids*, 1979, **34**, 127–136.

60 J. Yang, H. Liu, W. N. Martens and R. L. Frost, *J. Phys. Chem. C*, 2010, **114**, 111–119.

61 J.-K. Chang, C.-M. Wu and I.-W. Sun, *J. Mater. Chem.*, 2010, **20**, 3729–3735.